GEOPHYSICS, VOL. 78, NO. 2 (MARCH-APRIL 2013); P. R107–R124, 20 FIGS.
10.1190/GEO2012-0203.1

Which parameterization is suitable for acoustic vertical transverse isotropic full waveform inversion? Part 2: Synthetic and real data case studies from Valhall

Yaser Gholami[1], Romain Brossier[2], Stéphane Operto[3], Vincent Prieux[4], Alessandra Ribodetti[3], and Jean Virieux[2]

ABSTRACT

It is necessary to account for anisotropy in full waveform inversion (FWI) of wide-azimuth and wide-aperture seismic data in most geologic environments, for correct depth positioning of reflectors, and for reliable estimations of wave speeds as a function of the direction of propagation. In this framework, choosing a suitable anisotropic subsurface parameterization is a central issue in monoparameter and multiparameter FWI. This is because this parameterization defines the influence of each physical parameter class on the data as a function of the scattering angle, and hence the resolution of the parameter reconstruction, and on the potential trade-off between different parameter classes. We apply monoparameter and multiparameter frequency-domain acoustic vertical transverse isotropic FWI to synthetic and real wide-aperture data, representative of the Valhall oil field. We first show that reliable monoparameter FWI can be performed to build a high-resolution velocity model (for the vertical, the horizontal, or normal move-out velocity), provided that the background models of two Thomsen parameters describe the long wavelengths of the subsurface sufficiently accurately. Alternatively, we show the feasibility of the joint reconstruction of two wave speeds (e.g., the vertical and horizontal wave speeds) with limited trade-off effects, while Thomsen parameter δ is kept fixed during the inversion. The influence of the wave speeds on the data for a limited range of scattering angles when combined each other can, however, significantly hamper the resolution with which the two wave speeds are imaged. These conclusions inferred from the application to the real data are fully consistent with those inferred from the theoretical parameterization analysis of acoustic vertical transverse isotropic FWI performed in the companion report.

INTRODUCTION

Full waveform inversion (FWI) is a data-fitting approach that is theoretically amenable to inversion of the full wavefield recorded by wide-azimuth and wide-aperture acquisition geometries (see Virieux and Operto [2009] for a review). For such acquisitions, it can be critical to account for the intrinsic variations of the wave speed with the direction of propagation during the inversion; namely, the anisotropy. The footprint of anisotropy in FWI of wide-azimuth and wide-aperture acquisitions is shown by Plessix and Perkins (2010) and Prieux et al. (2011). Plessix and Perkins (2010) show how accounting for anisotropy in seismic modeling during FWI allows improvement of the FWI velocity model, which is subsequently used as the background model for reverse-time migration (RTM). The results of the RTM computed in the anisotropic FWI velocity model show flat common-image gathers (CIGs) below salt structures. Prieux et al. (2011) compare the results of isotropic and anisotropic acoustic FWI of wide-aperture ocean-bottom cable

Manuscript received by the Editor 1 June 2012; revised manuscript received 20 November 2012; published online 11 March 2013.
[1]Formerly Géoazur, Université Nice-Sophia Antipolis, CNRS, IRD, Observatoire de la Côte d'Azur, Sophia-Antipolis, France. Currently CGG-Veritas, London, U. K. E-mail: gholami@geoazur.unice.fr.
[2]ISTerre, Université Joseph Fourier, Grenoble, Observatoire des Sciences de l'Univers, Grenoble, France. E-mail: romain.brossier@obs.ujf-grenoble.fr; jean.virieux@ujf-grenoble.fr.
[3]Géoazur, Université Nice-Sophia Antipolis, CNRS, IRD, Observatoire de la Côte d'Azur, Sophia-Antipolis, France. E-mail: operto@geoazur.unice.fr; ribodetti@geoazur.unice.fr
[4]Formerly Géoazur, Université Nice-Sophia Antipolis, CNRS, IRD, Observatoire de la Côte d'Azur, Sophia-Antipolis, France. Currently CGG-Veritas, Massy, France. E-mail: prieux@geoazur.unice.fr.

(OBC) data from the Valhall field. When isotropic FWI is performed, they showed that horizontal velocities are reconstructed in the upper structure because FWI is mostly driven by the diving waves and the postcritical reflections, which have a direction of propagation close to horizontal. The reconstruction of the horizontal velocities in the upper structure leads to incorrect velocities in the underlying gas layers and mispositioning of the cap rock on the top of the reservoir level. These deep structures are mainly sampled by short-spread reflections, which are mostly sensitive to the normal move-out (NMO) and vertical velocities.

Most of the anisotropic FWI applications aim to update the vertical or NMO velocity, while keeping the Thomsen anisotropic parameters fixed (i.e., δ, ϵ or a combination of the two, as represented by the anellipticity parameter η [Alkhalifah and Tsvankin, 1995]) (Plessix and Perkins, 2010; Vigh et al., 2010; Prieux et al., 2011). Only a few attempts have been made to update multiple classes of parameters by anisotropic FWI during synthetic experiments in acoustic or elastic vertical transverse isotropic (VTI) approximations (Ji and Singh, 2005; Barnes et al., 2008; Lee et al., 2010; Plessix and Cao, 2011).

In the initial companion report (Gholami et al., 2013), we investigate which classes of parameter need to be selected for FWI, based on scattering pattern analysis. The scattering pattern can be viewed as the amplitude of the wavefield perturbation as a function of the scattering angle that is generated by a point model perturbation (Figure 1a). The model perturbation is applied to one parameter class at a time and each parameter class is normalized by the mean value of the parameter such that each parameter class has the same range of values. Therefore, the scattering pattern of one parameter represents the influence of this parameter on the data as a function of the scattering angle. Notice that the influence of one parameter on the data can change depending on the other parameters involved in the subsurface parameterization. In the current study, we continue this investigation through synthetic and real data case studies of 2D monoparameter and multiparameter acoustic VTI FWI. For the synthetic and real data case studies, the acquisition geometry represents a long-offset ocean-bottom survey, and the geologic target is the Valhall oil field, where significant anisotropy has been reported (Kommedal et al., 1997; Thomsen et al., 1997; Barkved and Heavey, 2003).

In the present study, we consider three kinds of parameterization: Type 1 parameterization combines one wave speed (the vertical, the horizontal, or the NMO velocity, V_{P0}, V_h, V_{NMO}, respectively) with two Thomsen parameters (Thomsen, 1986) (ϵ, δ, or their combination, parameter η [Alkhalifah and Tsvankin, 1995]). We note that long-spread reflection traveltimes in homogeneous acoustic VTI media are governed by the NMO velocity and η. With type 1 parameterizations, the wave speed has a dominant influence on the data for the full range of scattering angles, whereas δ has a minor influence on the data (Figure 1b). Thomsen parameter ϵ has a higher influence on the data than δ, and shows significant trade-off with the wave speed. Alternatively, two wave speeds, for example the vertical and horizontal velocities, and one Thomsen parameter, for example δ, can be used in the subsurface parameterization (referred to as type 2 parameterization). In this case, the two wave speeds have significant influence on the data for distinct ranges of scattering angles (Figure 1c). For example, the vertical velocity has influence on the small and intermediate scattering angles, whereas the horizontal velocity has influence on the intermediate and large scattering angles, when they are combined with each other in the parameterization. In this case, the trade-off between the two wave speeds should be manageable, although it exists at intermediate scattering angles (Gholami et al., 2013, their Figure 3e and 3f). However, the resolution with which the two velocity models are reconstructed will be hampered by the narrow range of scattering angles for which they have influence.

In the first part of this study, we briefly review the FWI algorithm that we use. A more detailed review is presented in Gholami et al. (2013). In the second part, we present the application of FWI to the synthetic Valhall model. We apply monoparameter and multiparameter FWI to the synthetic data using the type 1 and type 2 parameterizations. We first show that a reliable velocity model can be built by monoparameter FWI, provided that large-scale background models of the Thomsen parameters are available. We then show the feasibility of the joint update of two wave speeds when using type 2 parameterization, while Thomsen parameter δ is kept fixed during the inversion. As expected, the horizontal velocities are reconstructed with low resolution because their influence is confined to the large scattering angles when type 2 parameterization is considered. In the last part of this study, these inversion tests are applied to the real data from Valhall, and they confirm the conclusions inferred from the theoretical analysis shown in Gholami et al. (2013) and from the synthetic case study presented in this study.

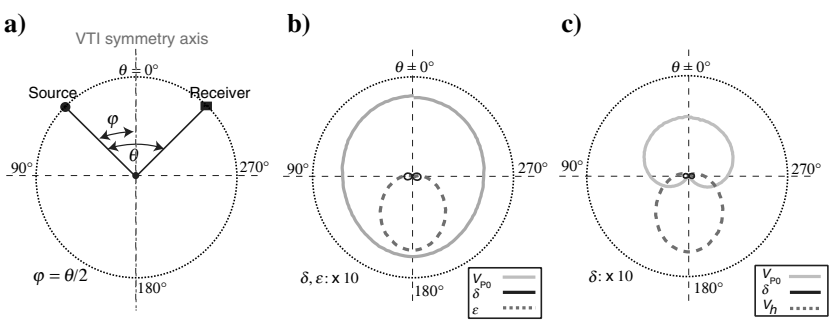

Figure 1. Scattering patterns for (V_{P0}, δ, ϵ) and (V_{P0}, δ, V_h) parameterizations. (a) The radiation patterns are shown for a specular reflection with respect to the vertical symmetry axis. This is representative of a surface-to-surface reflection from a horizontal interface. (b) (V_{P0}, δ,ϵ) parameterization. The lines represent the amplitude of a wavefield perturbation as a function of the scattering angle θ that is generated by a point perturbation of one parameter (V_{P0}, δ, ϵ, respectively). The parameter perturbation is a fixed percentage of the value of the parameter in the background medium. (c) Same as (b) for the (V_{P0}, δ, V_h) parameterization. Notice how the scattering pattern of the vertical velocity changes with the subsurface parameterization. See Gholami et al. (2013) for more details.

FULL-WAVEFORM INVERSION IN VERTICAL TRANSVERSE ISOTROPIC ACOUSTIC MEDIA

In the present study, we perform FWI in the frequency domain with the methodology described by Brossier (2011). A detailed review of the algorithm is presented in the companion paper (Gholami et al., 2013). Only a brief review is given here. Seismic modeling in VTI acoustic media is performed with a velocity-stress

discontinuous Galerkin finite-element method on unstructured triangular mesh (Brossier et al., 2008, 2010; Brossier, 2011). The acoustic approximation is implemented by setting the c_{44} elastic coefficient on the symmetry axis in the P-SV velocity-stress elastodynamic system to zero (Brossier et al., 2010). This gives

$$\begin{aligned} -\imath\omega v_x &= b\frac{\partial\sigma_{xx}}{\partial x}, \\ -\imath\omega v_z &= b\frac{\partial\sigma_{zz}}{\partial z}, \\ -\imath\omega\sigma_{xx} &= c_{11}\frac{\partial v_x}{\partial x} + c_{13}\frac{\partial v_z}{\partial z}, \\ -\imath\omega\sigma_{zz} &= c_{13}\frac{\partial v_x}{\partial x} + c_{33}\frac{\partial v_z}{\partial z}, \end{aligned} \tag{1}$$

where $\imath = \sqrt{-1}$ is the purely imaginary term, ω denotes the angular frequency, (v_x, v_z) and $(\sigma_{xx}, \sigma_{zz})$ are the particle velocities and *normal* stresses, respectively. In the framework of the acoustic approximation of VTI media, we shall consider the wavefield $\mathbf{p} = \frac{1}{2}(\sigma_{xx} + \sigma_{zz})$ as the pressure wavefield recorded by the hydrophone component. The subsurface is described by buoyancy b (the inverse of density), and the elastic moduli, c_{11}, c_{33}, and c_{13}.

Inversion is performed following a multiscale approach that proceeds sequentially over increasing frequencies, and is regularized with a Tikhonov regularization (Tikhonov and Arsenin, 1977).

We use the least-squares misfit function $\mathcal{C}(\mathbf{m})$ that is given by

$$\begin{aligned} \mathcal{C}(\mathbf{m}) &= \frac{1}{2}\Delta\mathbf{d}^{\dagger}\mathbf{W}_d\Delta\mathbf{d} \\ &\quad + \frac{1}{2}\sum_{i=1}^{N_p}\lambda_i(\mathbf{m}_i - \mathbf{m}_{\text{prior}_i})^{\dagger}\mathbf{W}_{m_i}(\mathbf{m}_i - \mathbf{m}_{\text{prior}_i}), \end{aligned} \tag{2}$$

where the expression $\Delta\mathbf{d} = \mathbf{d}_{\text{cal}}(\mathbf{m}) - \mathbf{d}_{\text{obs}}$ denotes the data residual vector, the difference between the modeled data $\mathbf{d}_{\text{cal}}(\mathbf{m})$ and the recorded data $\mathbf{d}_{\text{obs}}$. The $\dagger$ denotes the transpose (T) and complex conjugate ($*$) operators together. In the present study, we consider only the pressure wavefield recorded by the hydrophone component. The multiparameter subsurface model is denoted by $\mathbf{m} = (\mathbf{m}_1, \ldots, \mathbf{m}_{N_p})$, where N_p is the number of parameter classes to be updated during the FWI. The acoustic VTI medium is parameterized by three parameter classes: for example, the vertical velocity V_{P0} and Thomsen parameters δ and ϵ (Thomsen, 1986) and therefore $N_p \leq 3$. We assume that density and attenuation are known and are kept fixed during inversion. The source function is not included in our definition of the model parameters for the sake of compactness. The source function is estimated during the real data case study shown at the end of the present study by linear inversion (Pratt, 1999). The estimation of the source function with the adjoint state method in the framework of frequency-domain FWI is reviewed in Plessix and Cao (2011).

We minimize the misfit function with respect to model parameters that are normalized by their mean value in the background model: for example, $\mathbf{m}_1 = \mathbf{V}_{\text{P0}}/V_{\text{P0}_0}, \mathbf{m}_2 = \delta/\delta_0, \mathbf{m}_3 = \epsilon/\epsilon_0$, where V_{P0_0}, δ_0, and ϵ_0 denote the mean values of the subsurface parameters. This allows us to process multiple classes of parameter that have the same range of values. With this normalization, the parameter classes that have the dominant physical influence on the data have the Fréchet derivatives of highest amplitude (Gholami et al. [2013], their equation 13). Therefore, the model parameterization used in the present study tend to steer during FWI the model update toward those dominant parameters.

The weighting matrices $\mathbf{W}_{m_i}$ seek to penalize the roughness of the difference between the model $\mathbf{m}$ and the prior model $\mathbf{m}_{\text{prior}}$. The smoothing operators $\mathbf{W}_{m_i}^{-1}$ are exponential functions given by

$$\mathbf{W}_{m_i}^{-1}(z, x, z', x') = \sigma_i^2(z, x)\exp\left(\frac{-|x - x'|}{\tau_x}\right)\exp\left(\frac{-|z - z'|}{\tau_z}\right), \tag{3}$$

where τ_x and τ_z denote the horizontal and vertical correlation lengths, respectively, defined as a fraction of the local wavelength. The coefficient σ_i represents the standard error. As we minimize the misfit function with respect to normalized parameters, we use $\sigma_i = 1$ for all i. An exponential function is used for $\mathbf{W}_{m_i}^{-1}$ because its inverse in the expression of the misfit function, equation 2, can be computed analytically (Tarantola [1987], pages 308–310). Data preconditioning can be applied through the weighting matrix $\mathbf{W}_d$, which weights each component of the data-misfit vector. In this study, we shall use the identity for $\mathbf{W}_d$. Therefore, no data weighting is applied. The scalar hyperparameters λ_i control the respective weight of the data-space and model-space misfit functions in equation 2. Their values can be adapted to each parameter class.

The perturbation model that minimizes the misfit function at iteration k is given by

$$\begin{aligned} \Delta\mathbf{m}^{(k)} &= -\gamma^{(k)}\left[\frac{\partial^2 C(\mathbf{m}^{(k)})}{\partial\mathbf{m}}\right]^{-1}\frac{\partial C(\mathbf{m}^{(k)})}{\partial\mathbf{m}} \\ &= -\gamma^{(k)}\Re\left(\hat{\mathbf{W}}_m^{-1}(\mathbf{J}^{(k)})^{\dagger}\mathbf{W}_d\mathbf{J}^{(k)} + \hat{\mathbf{W}}_m^{-1}\left(\frac{\partial(\mathbf{J}^{(k)})}{\partial\mathbf{m}^T}\right)\right. \\ &\qquad \left.((\Delta\mathrm{d}^{(k)})^* \ldots (\Delta\mathrm{d}^{(k)})^*) + \Lambda\right)^{-1} \\ &\qquad \Re(\hat{\mathbf{W}}_m^{-1}(\mathbf{J}^{(k)})^T\mathbf{W}_d(\Delta\mathrm{d}^{(k)})^* + \Lambda(\mathbf{m}^{(k)} - \mathbf{m}_{\text{prior}})), \end{aligned} \tag{4}$$

with $\mathbf{m}^{(k+1)} = \mathbf{m}^{(k)} + \Delta\mathbf{m}^{(k)}$ and $\gamma^{(k)}$ is the step length estimated by line search. The first and second derivatives of the misfit function on the right side of equation 4 are the gradient and the Hessian of the misfit function, the expression of which are given as a function of the sensitivity or Fréchet derivative matrix $\mathbf{J}$.

In equation 4, Λ is a block diagonal damping matrix

$$\Lambda = \begin{pmatrix} \lambda_1\mathbf{I}_M & \ldots & 0 \\ \ldots & \ldots & \ldots \\ 0 & \ldots & \lambda_{N_p}\mathbf{I}_M \end{pmatrix}, \tag{5}$$

and $\mathbf{I}_M$ is the identity matrix of dimension M, where M denotes the number of model parameters per class. In equation 4, $\Re$ denotes the real part of a complex number. The matrix $\hat{\mathbf{W}}_m^{-1}$ is a $N_p \times N_p$ block diagonal matrix, where each block is formed by the $\hat{\mathbf{W}}_{m_i}^{-1}$ matrices. The gradient of the misfit function (Gholami et al. [2013], their Appendix B) is computed with the adjoint-state method (Plessix, 2006) and has the general form

$$\frac{\partial C(\mathbf{m}^{(k)})}{\partial m_{ij}} = \sum_{\omega}\sum_{s}\Re\left\{\hat{\mathbf{W}}_{m_i}^{-1}\mathbf{v}_{s,\omega}^T\left(\frac{\partial\mathbf{B}_{\omega}}{\partial m_{ij}}\right)^T\beta_{1_{s,\omega}}^*\right\}, \tag{6}$$

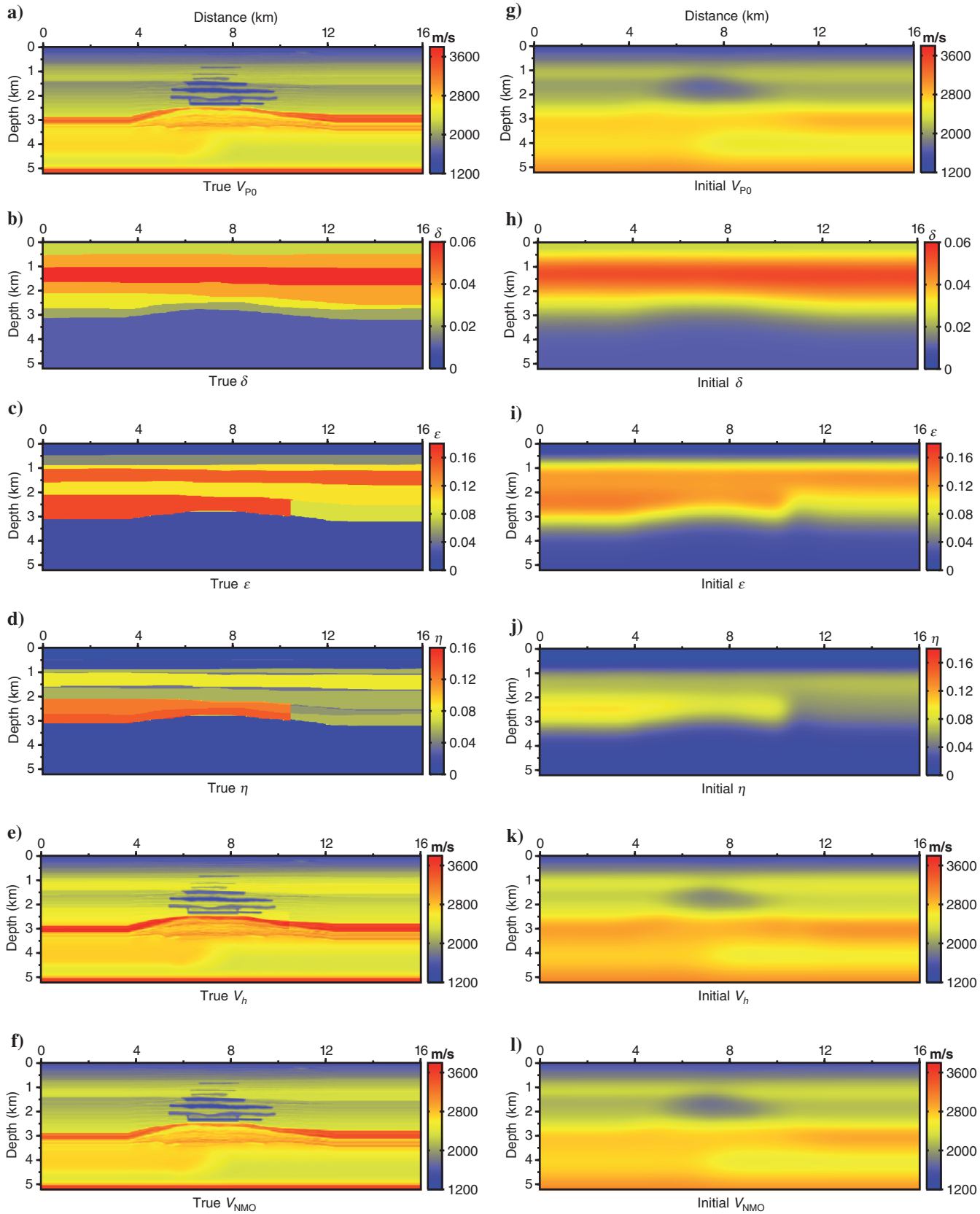

Figure 2. Valhall synthetic case study. (a) Vertical velocity model. (b, c) Models of Thomsen parameters δ (b) and ϵ (c). (d) Model of η. (e, f) Horizontal (e) and NMO (f) velocity models. (g, l) Same as (a, f) for the smooth initial FWI models.

where **B** is the forward-modeling operator, **v** is the particle velocity wavefield, and β_1 is the back-propagated adjoint wavefield (Gholami et al. [2013], their Appendix B). The indices i and j denote the ith parameter class and the jth parameter of class i. The coefficients of **B** depend on the frequency ω, and the wavefields **v** and β depend on the shot s and on the frequency ω. Summation in equation 6 is performed over frequencies ω and sources s. The operator $\frac{\partial \mathbf{B}}{\partial m_{ij}}$ is the scattering pattern of the virtual source of the so-called partial derivative wavefield (Pratt et al., 1998). The gradient of the misfit function can be derived for a reference parameterization, for example, the elastic moduli c_{11}, c_{33}, and c_{13} in equation 1, and the gradients of the misfit function for other parameterization are inferred by applying the chain law of partial derivatives to the scattering-pattern term.

We compute an approximation of the product of the inverse Hessian with the gradient in equation 4 with the limited-memory Broyden-Fletcher-Goldfard-Shanno (L-BFGS) quasi-Newton algorithm (Nocedal, 1980). As an initial guess of the inverse of the Hessian, we use a diagonal approximation of the approximate Hessian (the linear term) at the first iteration damped by the Λ matrix and smoothed by $\hat{\mathbf{W}}_m^{-1}$,

$$\mathbf{H}_0 = (\hat{\mathbf{W}}_m^{-1}\mathrm{diag}\{\mathbf{J}^{(1)^\dagger}\mathbf{W}_d\mathbf{J}^{(1)}\} + \Lambda). \tag{7}$$

REALISTIC SYNTHETIC VALHALL CASE STUDY

Model and data

The 2D synthetic Valhall velocity model (Figure 2a) is a realistic synthetic model that is inspired by the geology of the Valhall oil and gas field located in the North Sea (Munns, 1985; Leonard and Munns, 1987). The experimental setup of the synthetic Valhall inversion is performed as close as possible to the real-data case study, which will be discussed later. The vertical velocity model shows a series of horizontal gas layers between 1.5 and 2.5 km in depth, which hamper the imaging of the underlying reservoir at 2.5 km in depth (Kommedal et al., 1997; Thomsen et al., 1997; Barkved and Heavey, 2003). The δ and ϵ models are shown in Figure 2b and 2c. In some areas, the anisotropy is significant, with the horizontal velocity 15% higher than the vertical velocity as revealed by the values of the parameter η (Figure 2d). Time-domain synthetic seismograms computed in the true VTI model are shown

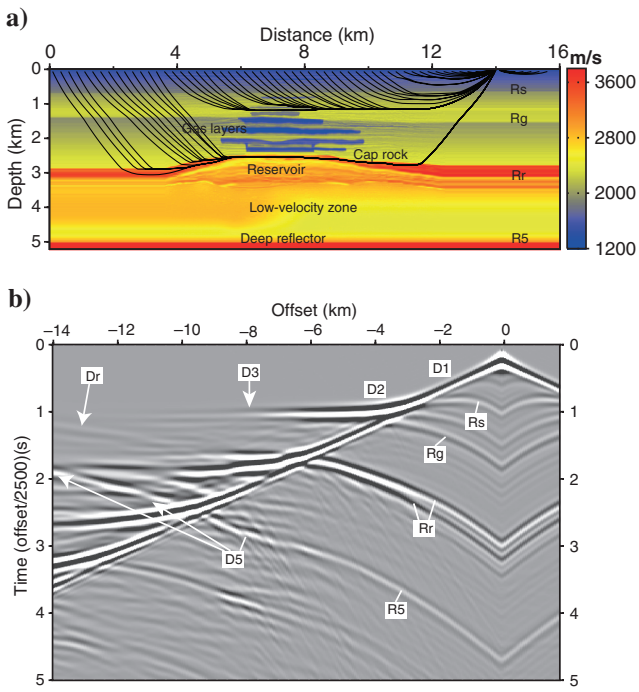

Figure 3. Valhall synthetic case study. (a) Main structural units: gas layers between 1400 and 2400 m in depth, the reservoir at 2500 m in depth, a flat reflector at 5000 m in depth. Isotropic first-arrival rays are superimposed on the model for a source at 14 km in distance. (c) Acoustic VTI synthetic seismograms computed in the models shown in (Figure 2a and 2c). The time axis is shown with a reduction velocity of 2.5 km/s. Phase nomenclature: D1, D2, D3: diving waves in the upper structure above the gas layers. Dr: head wave from the top of the reservoir. Rs: shallow reflection from the reflector located at around 700 m in depth. Rg: reflection from the top of the gas layers. Rr: reflections from the top and bottom of the reservoir. D5, R5: head wave and reflection from the interface located at 5000 m in depth.

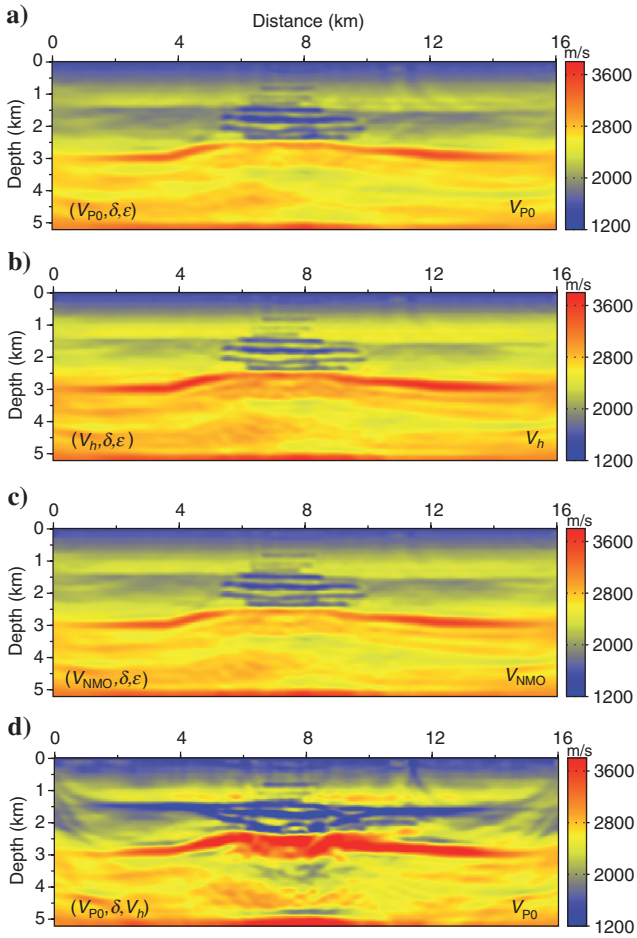

Figure 4. Monoparameter VTI FWI. (a-c) The vertical velocity model (a), the horizontal velocity model (b), and the NMO velocity model (c) are reconstructed by monoparameter FWI for the type 1 parameterization that combines one wave speed and two Thomsen parameters δ and ϵ. (d) The vertical velocity model is reconstructed by monoparameter FWI for the (V_{P0}, δ, V_h) parameterization.

in Figure 3b for a shot located at 14 km in distance. For phase interpretation, we compute isotropic first-arrival ray-tracing in the vertical velocity model (Figure 3a). First-arrival rays propagate in the upper structure above the gas layers and at the reservoir level. As the gas layers form on average a low-velocity zone with respect to the surrounding layers, no first-arrival rays pass through them. The main arrivals are diving waves that propagate above the gas layers (Figure 3b, D1, D2, D3), a weak-amplitude head wave from the top of the reservoir (Figure 3b, Dr), and a series of reflections from the upper sedimentary layers, the top of the gas layers, the top and bottom of the reservoir, and the high-velocity interface located at 5000 m in depth (Figure 3b, Rs, Rg, Rr, R5). The head wave that propagates along the deep interface at 5 km in depth is also visible as a secondary arrival (Figure 3b, D5). The data content suggests that the FWI reconstruction of the target above the gas layers will be driven by diving waves and precritical and postcritical reflections, whereas the reconstruction at the reservoir level will be dominated by precritical reflections. Although postcritical reflections from the reservoir level are shown, complex interactions of these phases with shingling multirefracted phases in the shallow part probably makes the inversion of the postcritical reflections from the reservoir more challenging. Because the upper target is sampled by waves that propagate with a wide range of directions, the footprint of the anisotropy is expected to be significant in this part of the target (Prieux et al., 2011).

Full waveform inversion setup

The acquisition geometry considered for FWI is representative of an OBC survey with receivers on the sea bottom at 71 m in depth (water depth is 70 m) and sources just below the water surface at 6 m in depth. Only the pressure wavefield (hydrophone component) is considered for the acoustic VTI inversion. The maximum offset in the acquisition is 15.7 km, which provides a wide-aperture surface data set. The shot and receiver spacings are 50 m. Five frequency components between 2 and 6 Hz (2, 3, 4, 5 and 6 Hz) are inverted successively with the quasi-Newton L-BFGS optimization method (Nocedal, 1980). Recorded and modeled data are damped in time from the first-arrival time t_0 with decaying exponential function $\exp^{-\alpha(t-t_0)}$ during each single-frequency inversion to inject progressively later-arriving phases in the inversion (Brossier et al., 2009). Three time dampings ($\alpha = 1/0.5,\ 1/3,\ 1/10\ \mathrm{s}^{-1}$) are successively used during each single-frequency inversion. Ten inversion iterations are performed per time damping, leading to a total number of 30 iterations per frequency. The starting models for inversion are built by Gaussian smoothing of true models (Figure 2g–2l).

The prior model in equation 2 is set to the initial model of the current iteration. This allows us to drop off the regularization term in the expression of the gradient in equation 4. In this case, the Tikhonov regularization reduces to a smoothing of the gradient and of the Hessian by the operator $\mathbf{W}^{-1}$, equation 4, and to the damping of the Hessian by the diagonal matrix Λ. We use a vertical and horizontal correlation length of 60 m for the smoothing of the gradient and Hessian, for each frequency and each parameter class. We also use the same value for λ_i, whatever the parameter class i. This value, denoted by λ is set to 1% of the maximum diagonal coefficient of the approximate Hessian $\mathbf{J}^t\mathbf{J}$, equation 4. It is remembered that we minimize the misfit function with respect to model parameters that are normalized by their mean value in the background model. As discussed in Gholami et al. (2013), this normalization makes the parameters with the strongest physical influence on the data to have the Fréchet derivatives of highest amplitudes. If

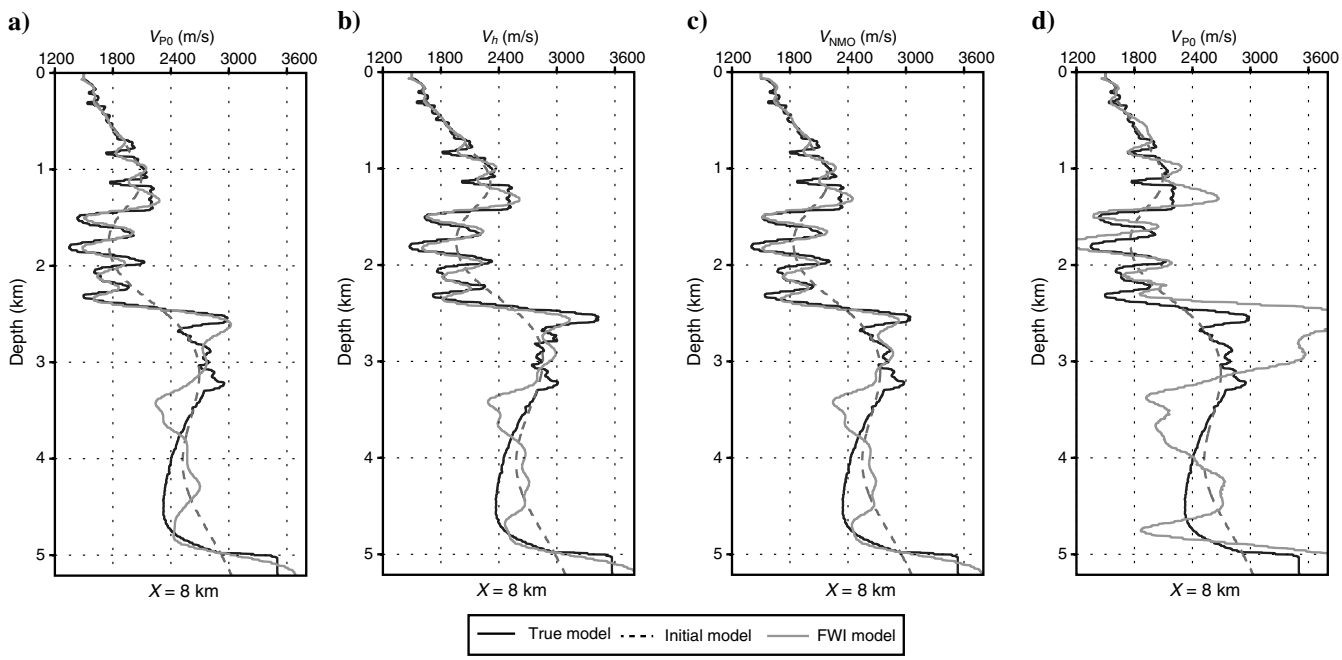

Figure 5. Vertical logs of the FWI models shown in Figure 4. The log is located at 8 km in distance in the middle of the model. The logs of the true model and of the initial models are plotted with solid black and dash gray lines, respectively. (a) Vertical velocity FWI model for the (V_{P0}, δ, ϵ) parameterization. (b) Horizontal velocity FWI model for the (V_h, δ, ϵ) parameterization. (c) NMO velocity FWI model for the (V_{NMO}, δ, ϵ) parameterization. (d) Vertical-velocity FWI model for the (V_{P0}, δ, V_h) parameterization.

the influence of the secondary parameters is one order of magnitude lower than that of the dominant parameter, the prewhitening factor in the Hessian can prevent the correct scaling of the gradient of the secondary parameters. This can lead to underestimation of these model perturbations. Clearly, we tune the inversion such that the results are steered toward the reconstruction of the parameters with the strongest influence on the data. Intensive investigation of other FWI setup remains out of the scope of this study. Nevertheless, we will show under which conditions this specific tuning provides satisfying results for type 1 and type 2 parameterizations.

Following Gholami et al. (2013), we consider two kinds of subsurface parameterizations in the present study. The first parameterization consists of one wave speed (vertical velocity, horizontal velocity, and NMO velocity) and two Thomsen parameters δ and ϵ. The second one combines two wave speeds (for example, the horizontal and vertical wave speeds) with the Thomsen parameter δ.

It is remembered that the horizontal (V_h) and NMO (V_{NMO}) velocities are related to the vertical velocity and the dimensionless Thomsen's parameters δ and ϵ by

$$V_{\mathrm{NMO}} = V_{\mathrm{P0}}\sqrt{1+2\delta} \quad V_h = V_{\mathrm{P0}}\sqrt{1+2\epsilon}. \tag{8}$$

Monoparameter anisotropic full waveform inversion

We first consider the type 1 parameterization that consists of one wave speed (vertical velocity, horizontal velocity, and NMO velocity) and two Thomsen parameters δ and ϵ. We showed in Gholami et al. (2013) that, for this kind of parameterization, the wave speed has a dominant influence on the wavefield for the full range of scattering angles (Figure 1b). The Thomsen parameter δ is the parameter with the most negligible influence on the data at intermediate scattering angles. The Thomsen parameter ϵ has an influence on the data at large-to-intermediate scattering angles, when ϵ is associated with the vertical velocity in the subsurface parameterization. As the wave speed has a dominant influence on the wavefield for the full range of scattering angles, tradeoff exists between the vertical wave speed and ϵ at large-to-

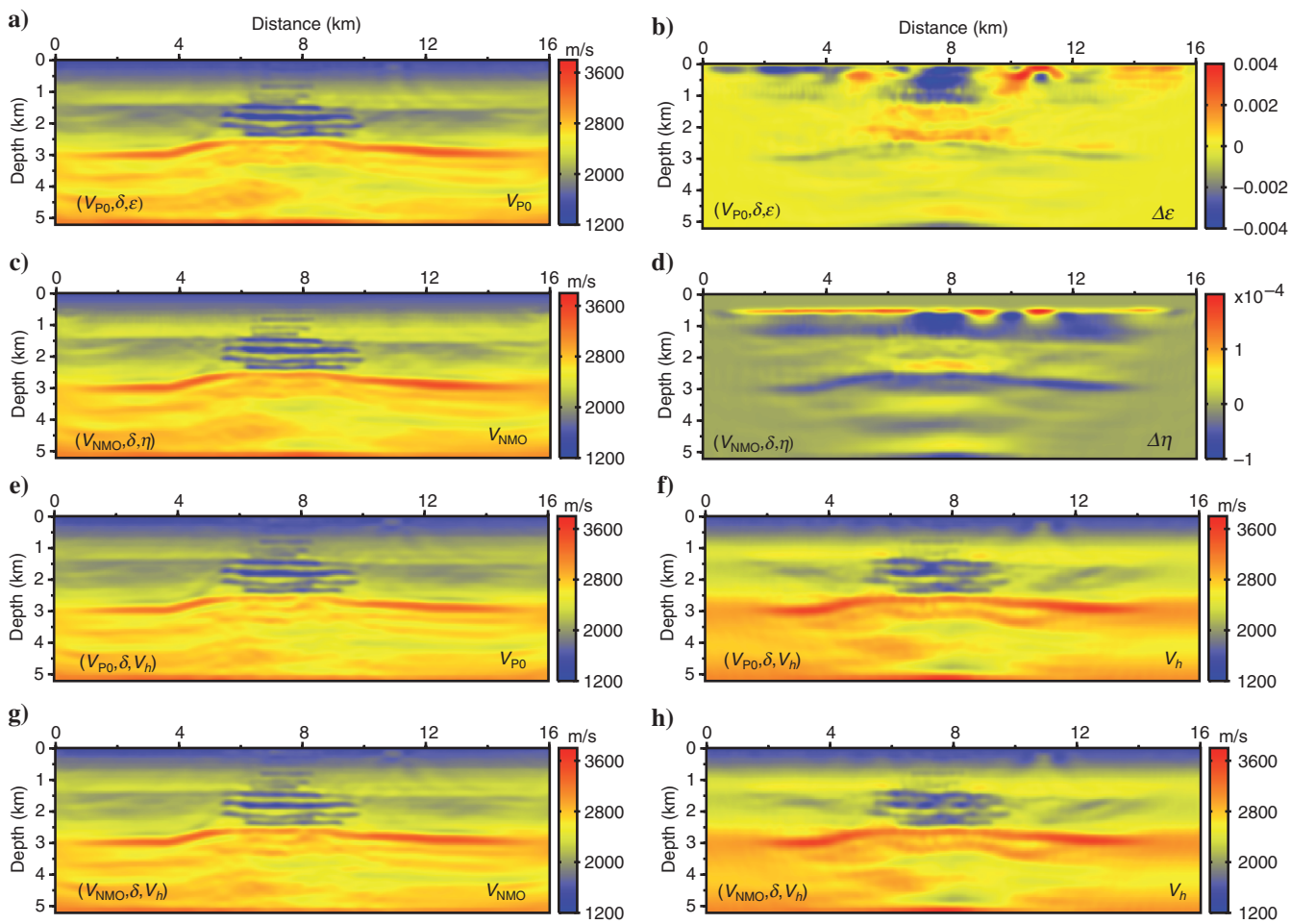

Figure 6. Multiparameter anisotropic FWI. (a, b) Joint update of the vertical velocity (a) and the Thomsen parameter ϵ (b) for the (V_{P0}, δ, ϵ) parameterization. Note that we show the difference between the final and initial ϵ models rather than the final ϵ model because the final ϵ model and the initial ϵ model are quite close. (c, d) Joint update of the NMO velocity (c) and η (d) for the (V_{NMO}, δ, η) parameterization. As for ϵ, we show the difference between the final η model and the initial η model. (e, f) Joint update of the vertical velocity (e) and of the horizontal velocity (f) for the (V_{P0}, δ, V_h) parameterization. (g-h) Joint update of the NMO velocity (g) and of the horizontal velocity (h) for the (V_{NMO}, δ, V_h) parameterization.

intermediate scattering angles. According to the dominant influence of the wave speed on the wavefield, a possible strategy is to first perform a monoparameter FWI to reconstruct a high-resolution model of the wave speed, keeping the δ background model and the ϵ background model fixed. For doing so, we shall first assume that the background models that describe the long wavelengths of δ and ϵ are available (Figure 2h and 2i), and that all of the data residuals mainly result from missing vertical velocity perturbation rather than missing δ and ϵ perturbations. This latter assumption is justified for ϵ because the data are only sensitive to the long wavelengths of ϵ, and these wavelengths are already present in the background model. The final models of the monoparameter FWI for the vertical velocity, for the horizontal velocity, and for the NMO velocity are shown in Figure 4a–4c. Comparisons between the logs extracted from the true models and from the FWI models show that reliable velocity models are obtained for each parameter-

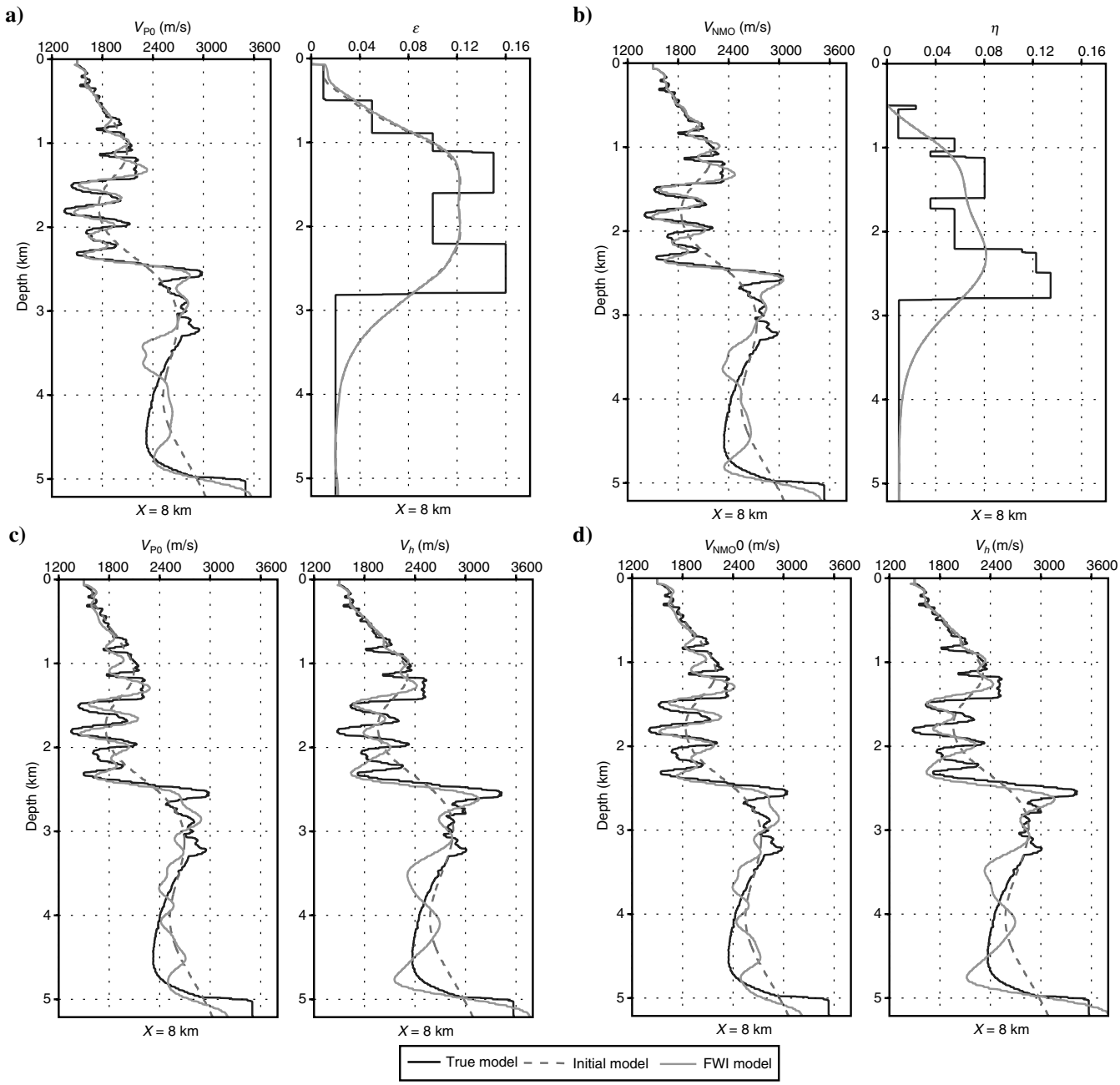

Figure 7. Vertical logs of multiparameter FWI models (solid gray line) shown in Figure 6. The true model and the initial model are plotted with solid black and dashed gray lines, respectively. The log is taken at 8 km in distance in the middle of the model. (a) Vertical velocity logs (left) and ϵ logs (right) extracted from the models of Figure 6a and 6b. (b) Vertical velocity logs (left) and η logs (right) extracted from the models of Figure 6c and 6d. (c) Vertical velocity log (left) and horizontal velocity log (right) extracted from the models of Figure 6e and 6f. (d) NMO velocity log (left) and horizontal velocity log (right) extracted from the models of Figure 6g and 6h.

ization (Figure 5a–5c). These results confirm that prior knowledge of the long wavelengths of δ and ϵ can be sufficient to build high-resolution velocity models by monoparameter anisotropic FWI. For highlighting the sensitivity of the monoparameter FWI to the subsurface parameterization, we perform monoparameter FWI for the vertical velocity using the (V_{P0}, δ, V_h) parameterization instead of the (V_{P0}, δ, ϵ) parameterization (Figure 4d). The initial model for the horizontal velocity is shown in Figure 2k, and it is built from the smooth background model of the vertical velocity (Figure 2g) and from the smooth background model of ϵ (Figure 2i). Therefore, the data residuals at the first iteration of the inversion performed with the type 1 and type 2 parameterizations are identical: Differences in the FWI results will be only due to the parameterization. Poor reconstruction of the vertical velocity with overestimated perturbations is shown for the type 2 parameterization (Figures 4d and 5d). The poor reconstruction of the vertical velocity results because data residuals at wide scattering angles can be only reduced by horizontal-velocity updates. Moreover, vertical-velocity and horizontal-velocity updates are necessary to cancel the data residuals at intermediate scattering angles. This is shown by the radiation pattern of the type 2 parameterization (Figure 1c) which show a maximum sensitivity of the wide-aperture data to the horizontal velocity and potential trade-off between vertical and horizontal wave speeds at intermediate scattering angles. As the smooth horizontal velocity background model is kept fixed, the data residuals at intermediate scattering angles have been erroneously interpreted as vertical velocity perturbations. This highlights on the one hand the trade-off that exists between vertical and horizontal velocities at intermediate scattering angles and the significant influence of the horizontal wave speed on the data when type 2 parameterization is used (Figure 1c).

Joint multiparameter anisotropic full waveform inversion

We now apply multiparameter FWI for joint reconstruction of two anisotropic parameters, while the smooth background model of δ is kept fixed during the FWI iterations due to its small influence on the data (Figure 6). The initial models are the smooth background models shown in Figure 2g–2l. We first update the vertical velocity and parameter ϵ using parameterization (V_{P0}, δ, ϵ). In this case, the vertical velocity model is slightly improved, in particular at the reservoir level, compared to the model obtained by monoparameter FWI (compare Figures 4a and 6a and Figures 5a and 7a). The ϵ model is weakly updated by FWI accordingly (Figures 6b and 7a), which is consistent with the reliable reconstruction of the vertical velocity performed by the monoparameter FWI. The weak perturbation of ϵ is justified because the data are sensitive to the long wavelengths of the parameter ϵ only, when the parameterization (V_{P0}, δ, ϵ) is used (Figure 1b). These long wavelengths are already accurately represented in the initial model. We also perform the joint update of the NMO velocity and η using the (V_{NMO}, δ, η) parameterization (Figures 6c, 6d, and 7b). The results show the same trend as for the (V_{P0}, δ, ϵ) parameterization: the velocity model is updated with high resolution, whereas the η model is kept almost unmodified. The negligible perturbation of parameter η, which is even smaller than that of parameter ϵ, is consistent with the smaller influence of parameter η relative to parameter ϵ for large scattering angles (Gholami et al. [2013], their Figure 3b and 3c). This smaller influence of parameter η for large scattering angles is balanced by the greater influence of parameter δ at small scattering angles when the (V_{P0}, δ, η) parameterization is used. The greater influence of parameter δ for this parameterization, which is kept

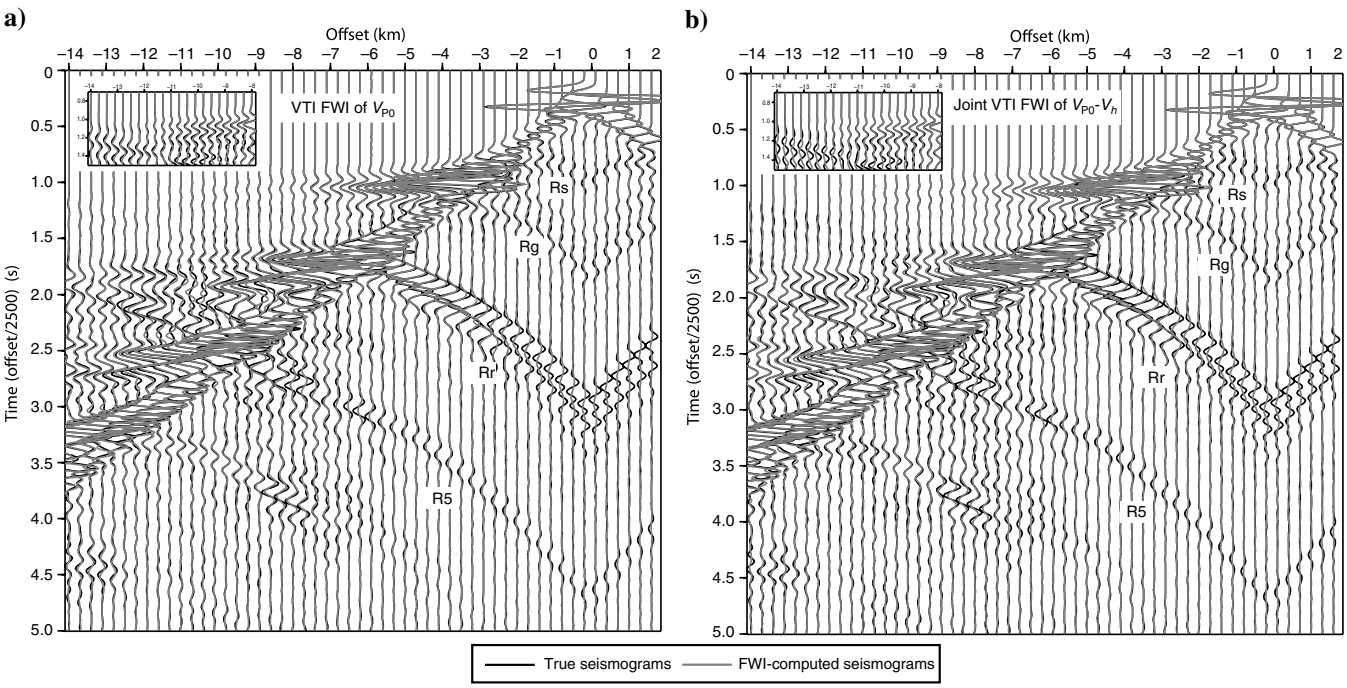

Figure 8. Direct comparison between synthetic seismograms computed in the multiparameter FWI models (gray lines) and in the true model (black lines). (a) Seismograms computed in the FWI models of Figure 6a and 6b ([V_{P0}, δ, ϵ] parameterization). (b) Seismograms computed in the FWI models of Figure 6c and 6d ([V_{P0}, δ, V_h] parameterization).

fixed during the inversion, does not impact on the reconstruction of the NMO velocity in Figure 6c.

The results of multiparameter FWI performed with the (V_{P0}, δ, V_h) and (V_{NMO}, δ, V_h) parameterizations confirm that two wave speeds (V_{P0} plus V_h and V_{NMO} plus V_h, respectively) can be jointly updated during FWI (Figure 6e–6h and Figure 7c–7d). The feasibility of the joint reconstruction of the two wave speeds is consistent with the radiation patterns of the two wave speeds when combined with each other in the subsurface parameterization, which shows a significant influence of the two wave speeds on the data for a nearly nonoverlapping band of scattering angles (Figure 1c). The vertical velocity model and the NMO velocity model are, however, less accurate than those inferred from the type 1 parameterization ([V_{P0}, δ, ϵ] and [V_{NMO}, δ, ϵ]) in particular in the shallow part of the medium where the scattering angle illumination is broad (compare Figure 6a and 6e, Figure 6c and 6g, and Figure 7a and 7c, Figure 7b and 7d). Moreover, the FWI horizontal velocity model has a low wavenumber content, and hence lacks resolution (Figure 6f, 6h, and Figure 7c, 7d). These two results are again consistent with the radiation pattern analysis presented in Gholami et al. (2013): The vertical velocity or the NMO velocity has a radiation pattern that spans over the full range of scattering angles when combined with the two Thomsen parameters in the subsurface parameterization (Gholami et al. [2013], their Figure 3b and 3d, gray curve), which leads to high-resolution reconstruction of the velocity field, whereas the radiation pattern has a narrower coverage centered on the short-scattering angles when the vertical velocity or the NMO velocity are associated with the horizontal velocity in the subsurface parameterization (Gholami et al., 2013, their

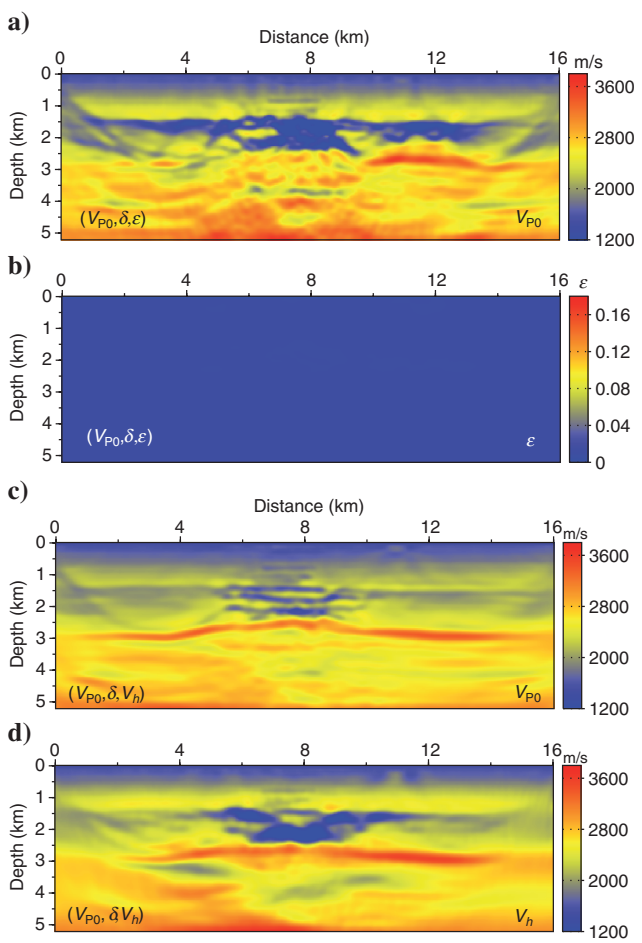

Figure 9. Multiparameter VTI FWI for vertical velocity (a) and ϵ (b) when the initial background models of ϵ and δ are homogeneous ($\epsilon = \delta = 0.01$). (c-d) Same as (a-b) for vertical velocity (c) and horizontal velocity (d).

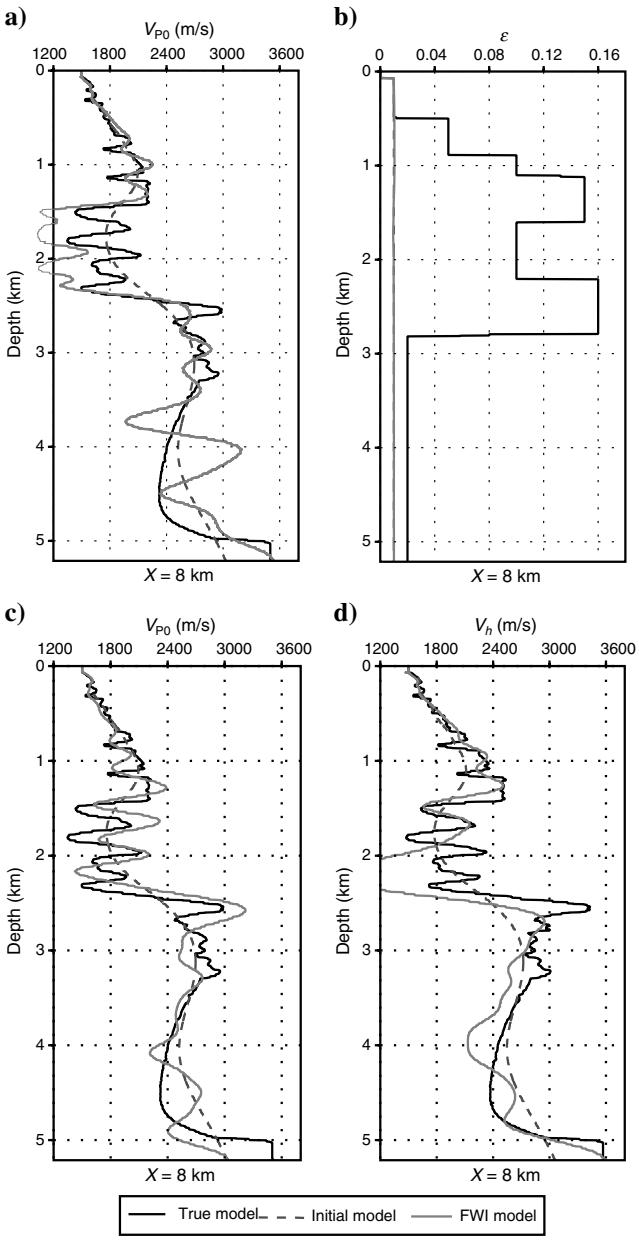

Figure 10. Logs of the V_{P0} FWI model (a) and the ϵ FWI model (b) (solid gray lines) shown in Figure 9a, 9b. The true and the initial models are plotted with solid black and dashed gray lines, respectively. The log is taken at 8 km in distance in the middle of the model. Note the strong underestimation of the vertical velocity in the gas layers. (c-d) Logs of the V_{P0} model (c) and the V_h model (d) shown in Figure 9c, 9d.

Figure 3e and 3f, gray curve). The lack of resolution of the horizontal velocity model is consistent with the radiation pattern of the horizontal velocity in the (V_{P0}, δ, V_h) and (V_{NMO}, δ, V_h) parameterizations. The influence of the horizontal velocity for large scattering angles governs the long-wavelength reconstruction of the subsurface (Gholami et al. [2013], their Figure 3e and 3f).

The seismograms computed in the final multiparameter FWI models obtained with the (V_{P0}, δ, ϵ) and (V_{P0}, δ, V_h) parameterizations show similar agreement with the seismograms computed in the true model (Figure 8).

Up to this point, we have assumed that smooth background models of the Thomsen parameters were available to perform monoparameter FWI and multiparameter FWI. We now consider the case where the initial models of δ and ϵ are homogeneous, with values $\delta = \epsilon = 0.01$, with the aim to increase the influence of the Thomsen parameters in the data residuals, and hence to create a more suitable configuration for retrieving them. We first perform the joint update of the vertical velocity and parameter ϵ with the (V_{P0}, ϵ, δ) parameterization (Figure 9a and 9b). The ϵ model remains unchanged, whereas the vertical velocities are strongly underestimated in the gas layers (Figure 10a and 10b). This highlights, on the one hand, the trade-off between the vertical velocity and parameter ϵ, and on the other hand, the dominant influence of the vertical velocity in the inversion. Remember that this dominant influence in the inversion results from the combined effects of the parameter normalization and the dominant imprint of the wave speeds on the data relatively to the Thomsen's parameters. Indeed, a more suitable tuning of the regularization, the aim of which is to preserve the scaling effect of the Hessian on the gradient of the misfit function, might allow a better scaling of the model perturbations of V_{P0} relative to those of parameter ϵ. Again, this is a difficult issue, which requires extensive trial-and-error and remains beyond the scope of the present study. The vertical velocity and parameter ϵ are underestimated in the final FWI models, in particular in the gas layers (Figure 10a and 10b), which leads to a severe underestimation of the horizontal velocities. Therefore, errors in the vertical velocity and parameter ϵ do not appear to compensate each other, but appear to accumulate their effects. This strongly indicates that the inversion is also hampered by cycle-skipping artifacts and remains locked into a local minimum because of the insufficient accuracy of the Thomsen parameter background models. This is supported by noting that the maximum difference between ϵ in the true model and the initial model is of the order of 0.15 between 1.2 and 1.5 km in depth and between 2.2 and 2.8 km in depth. This would lead to a traveltime error of the order of 0.75 s for a horizontally propagating wave, a mean vertical wave speed of 2 km/s, and an offset of 10 km. This is higher than half the period (0.25 s) of the starting frequency (2 Hz) in the inversion.

The results of multiparameter FWI performed with the (V_{P0}, δ, V_h) parameterization are shown in Figure 9c, 9d and Figure 10c, 10d. The initial V_h model is built from the initial smooth V_{P0} model (Figure 2g) and the homogeneous ϵ model. Therefore, the starting models used with the type 1 and type 2 parameterizations have the same kinematic accuracy. Compared to the results of the inversion obtained with parameterization (V_{P0}, δ, ϵ), the amplitude of the perturbations are of the same order of magnitude in the V_{P0} and V_h FWI models, with a lack of resolution on the V_h model. This is consistent with the former results obtained with the same parameterization (Figure 6e and 6f): The V_{P0} and V_h parameters have an

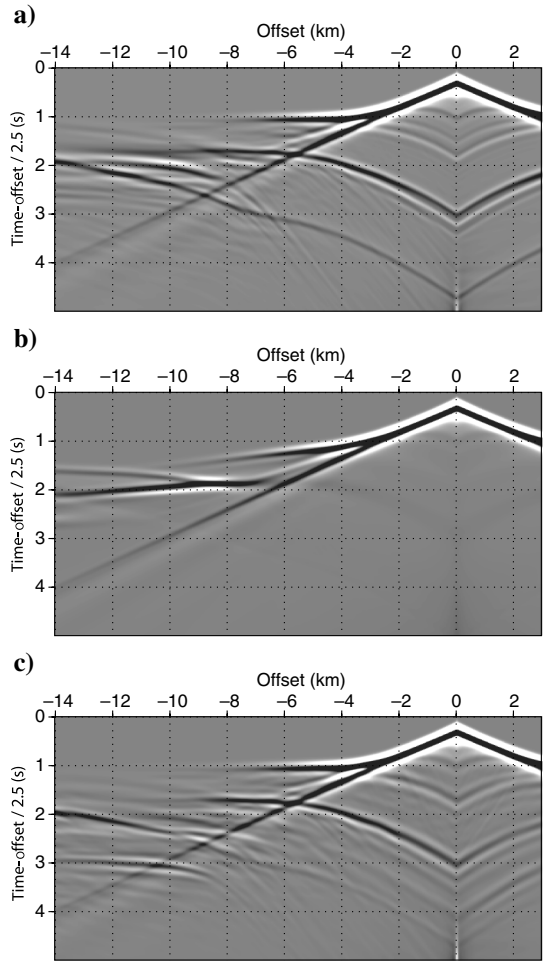

Figure 11. Seismogram modeling. (a) Seismograms computed in the true models. (b) Seismograms computed in the initial smooth vertical velocity model (Figure 2g) and in the constant δ and ϵ models ($\delta = \epsilon = 0.01$). (c) Synthetic seismograms computed in the FWI models of Figure 9c and 9d. Notice cycle-skipping artifacts beyond 8 km of offset.

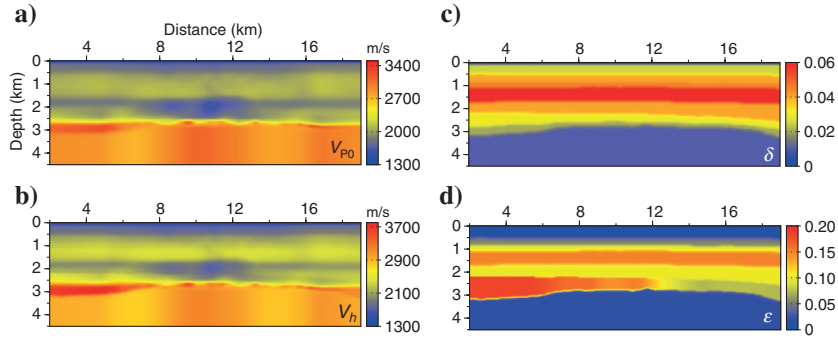

Figure 12. Valhall case study: initial FWI models. (a) Vertical velocity (V_{P0}), (b) horizontal velocity (V_h), (c) Thomsen parameter δ, (d) Thomsen parameter ϵ. The V_{P0}, δ, and ϵ models were built by reflection traveltime tomography (courtesy of BP).

influence in the data of the same order of magnitude but for distinct range of scattering angles. The footprint of the cycle-skipping artifacts takes the form of reflector mispositioning in the vertical velocity model and strongly underestimated horizontal velocities in the gas layers (Figure 10c and 10d).

Seismograms computed in the true models, in the initial models, and in the final FWI models obtained with type 2 parameterization are shown in Figure 11. Significant misfits at long offsets between the seismograms computed in the true model and the FWI model confirm that the FWI results were hampered by cycle-skipping artifacts.

APPLICATION TO REAL VALHALL DATA

We test the conclusions inferred from the synthetic experiments against the application of 2D visco-acoustic VTI FWI to the hydrophone component of an OBC data set recorded in the Valhall oil and gas field. The Valhall field is an overpressured, undersaturated, upper Cretaceous chalk reservoir located in the North Sea, approximately 290 km offshore of southern Norway, with a water depth of 69 m. The field is located in the most southwestern corner of the Norwegian continental shelf (Barkved and Heavey, 2003). This shallow-water field is characterized by a gas cloud above the reservoir, which hampers the imaging of reflectors at the oil reservoir level to 2.5 km in depth (Sirgue et al., 2010). The significant intrinsic anisotropy with a vertical velocity that is 15% slower than the horizontal velocity in some areas is another characteristic of this field (Kommedal et al., 2004). In the present study, we consider the cable 21 of the 3D, 4C data sets, which has been processed previously by 3D, isotropic acoustic FWI (Sirgue et al., 2010) and by 2D, isotropic and anisotropic FWI (Prieux et al., 2011). The footprint of anisotropy on the isotropic FWI was shown for this data set by Prieux et al. (2011). This line is located next to the gas cloud, which is highlighted by the horizontal slice of the 3D FWI model of Sirgue et al. (2010) at 1 km in depth (Prieux et al., 2011, their Figure 1). The shot and receiver spacings were 50 m. The maximum offset in the acquisition was 13 km. The 2D section along the position of cable 21 through the anisotropic 3D model of the Valhall field is shown in Figure 12. The anisotropic models for V_{P0}, δ and ϵ

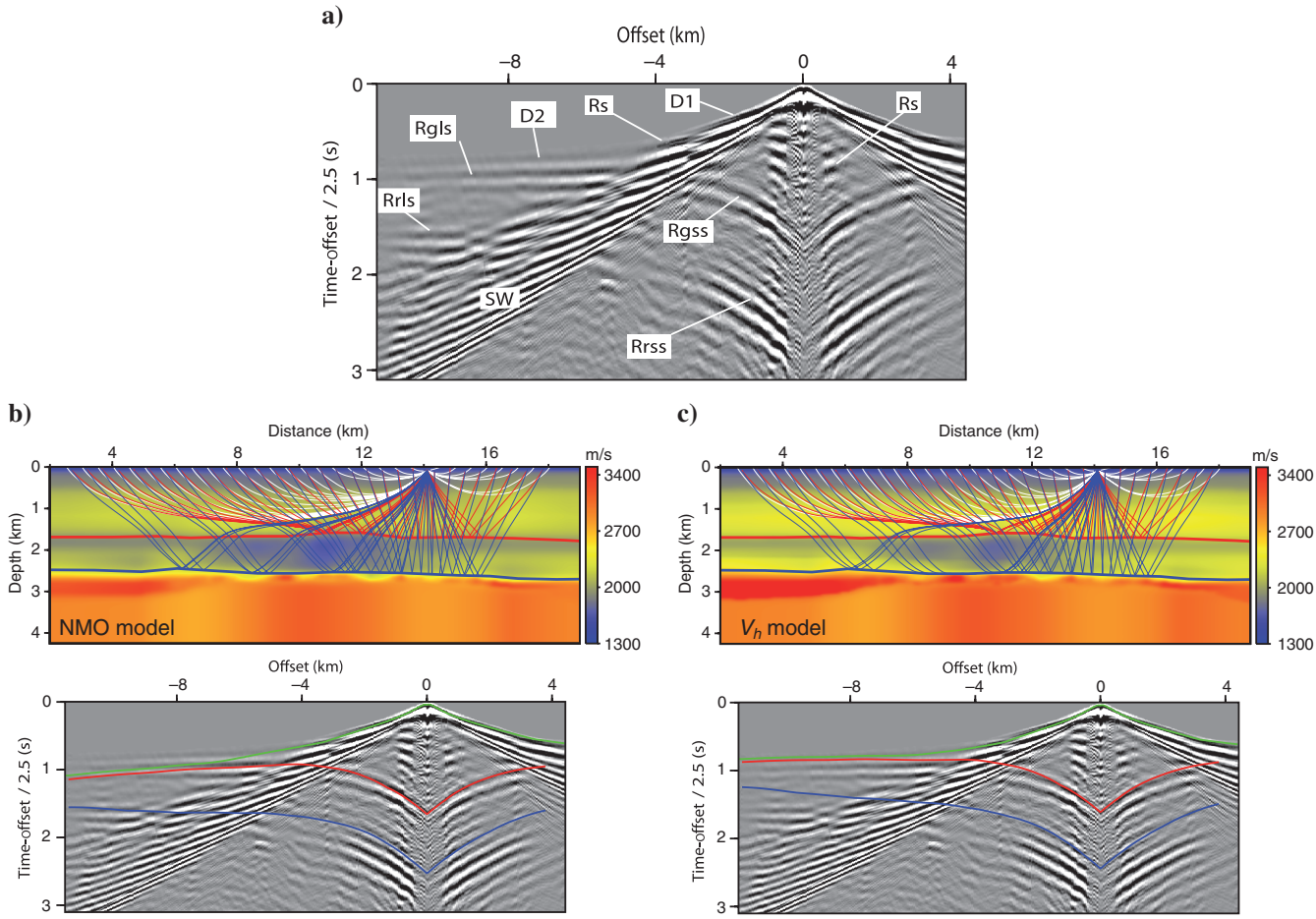

Figure 13. Valhall case study: data anatomy. (a) Example of preprocessed recorded receiver gather, at position $x = 14,100$ m. The vertical axis is plotted with a reduction velocity of 2.5 km/s. Phase nomenclature: D1, D2: diving waves. Rs: shallow reflection. Rgss / Rgls: short-spread and long-spread reflections from the top of the gas. Rrss / Rrls: short-spread and long-spread reflections from the top of the reservoir. SW: shingling waves. (b) Top: ray tracing in the NMO velocity model for the first arrival (white rays), and the reflections from the top of the gas (red) and the reservoir (blue). The green lines superimposed on the shot gather delineate computed first-arrival traveltimes, while the red and blue lines delineate the reflection traveltimes from the top of the gas and from the reservoir, respectively. Bottom: receiver gather shown in (a) with superimposed traveltime curves computed in the NMO model for these three phases. (c) As for (b), for the horizontal velocity model (from Prieux et al., 2011).

were built by reflection travel-time tomography (courtesy of BP), and they are used as the initial model for the VTI FWI in this study. The horizontal and NMO velocities are inferred from V_{P0}, δ and ϵ using equation 8.

A receiver gather for the hydrophone component at position $x =$ 14.1 km is shown in Figure 13a. The first arrivals (Figure 13a, D1, D2), the reflection from the top of the gas layer (Figure 13a, Rg), the reflection from the base of the gas layers, and the reflection from the top of the reservoir (Figure 13a, Rr) are highlighted in the seismograms. The reflections from the top of the reservoir are disrupted at critical and supercritical distances by shingling dispersive guided waves propagated in the near surface (Figure 13a, SW) (Robertson et al., 1996). We compute the first-arrival traveltimes and the reflection traveltimes from the top and the bottom of the gas layers in the NMO and horizontal velocity models using the isotropic eikonal solver of Podvin and Lecomte (1991) (Figure 13b and 13c), to check the kinematic accuracy of these velocities against the direction of propagation. The first-arrival rays do not sample the structure at the reservoir level, as they only travel down to 1.5 km in depth at their farthest offset. Superimposition of the computed traveltime curves on the receiver gather shows that the NMO velocities do not allow the traveltimes of diving waves at long offsets and the long-spread reflection Rg to be matched (Figure 13b). The traveltime delay exceeds half of the period of a starting frequency of 3.5 Hz, which prevents the criterion required to avoid cycle skipping to be satisfied. In contrast, the NMO velocity model is expected to match the short-spread reflection traveltimes of phases Rg and Rr, which is supported by Figure 13b. The horizontal velocity model allows for much better agreement of the first-arrival traveltimes (Figure 13c). However, the horizontal velocity model less accurately matches the reflection traveltimes at intermediate offsets, which highlights the footprint of the anisotropy in this data set. We apply VTI FWI to this OBC data set. Following the FWI set-up of Prieux et al. (2011), we successively invert five frequency groups: [3.5, 3.78, 4], [4, 4.3, 4.76], [4.76, 5, 5.25], [5.25, 5.6, 6], and [6, 6.35, 6.7] Hz with 25 iterations per frequency group. The density model is inferred from the initial V_{P0} model using the Gardner's law (Gardner et al., 1974). A homogeneous attenuation model was defined by trial-and-error, such that the root-mean-square amplitudes of the early arriving phases computed in the initial model roughly match those of the recorded data (Prieux et al., 2011). Prieux et al. (2011) reported a value of 150 for the best-fitting attenuation factor Q_P. The density and the attenuation models are kept fixed during the FWI iterations. Unlike for the synthetic example, we do not apply time damping to the data during the inversion of the real data. Time dampings did not increase the value of the FWI results for this real case study. This might result because the reflection wavefield carries out most of the information on the missing heterogeneities in the starting model, and as such it needs to be involved from the early stages of the inversion. The prior model is set as the starting model of each frequency group inversion,

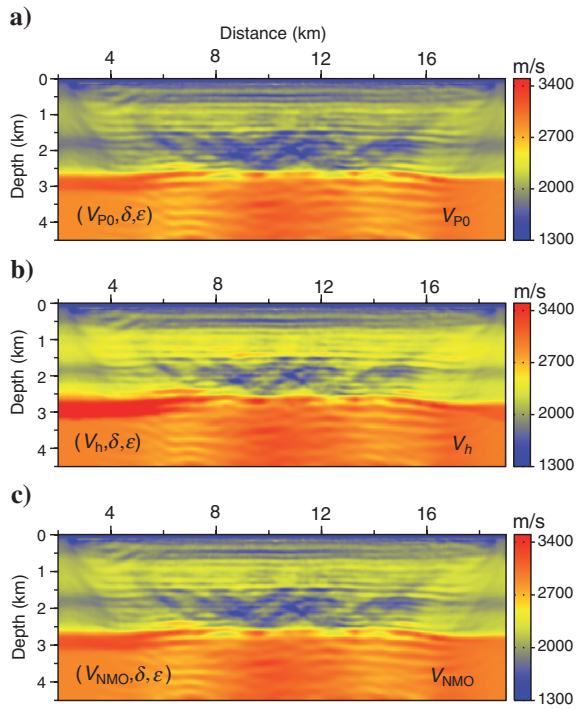

Figure 14. Valhall case study: final models of monoparameter FWI. (a) Vertical velocity model. (b) Horizontal velocity model. (c) NMO velocity model. The model space is parameterized by one wave speed (a) V_{P0}, (b) V_h, (c) V_{NMO}, and Thomsen's parameters δ and ϵ, these latter are kept fixed during inversion.

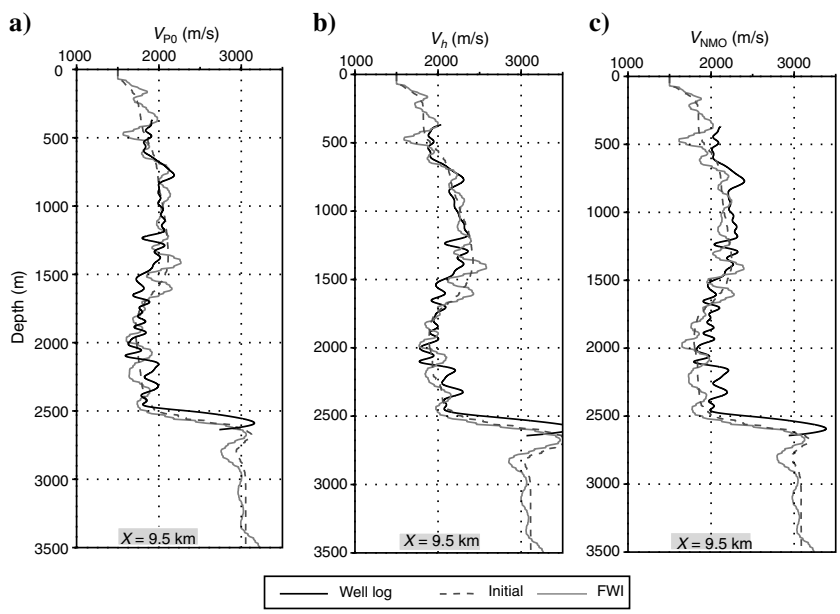

Figure 15. Valhall case study: Comparison between well log (black line) and FWI velocities (solid gray line). Log of the initial FWI models is plotted with dashed gray line. The sonic log has been smoothed according to the theoretical resolution of FWI (Prieux et al., 2011). (a) Vertical velocity. (b) Horizontal velocity. (c) NMO velocity. In (b) and (c), the well log for horizontal and NMO velocity were built from the original well log for vertical velocity (a) and the background δ and ϵ models.

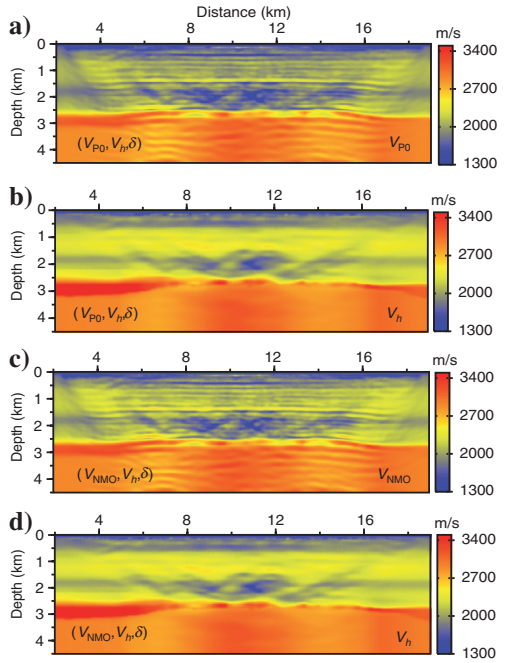

Figure 16. Valhall case study: Final models of multiparameter FWI. (a, b) Joint update of the vertical velocity (a) and the horizontal velocity (b) with the (V_{P0}, δ, V_h) parameterization. (c, d) Joint update of the NMO velocity (c) and of the horizontal velocity (d) with the (V_{NMO}, δ, V_h) parameterization. The smooth δ background model is kept fixed during FWI in both cases (Figure 12c). Note that the vertical oscillations in the upper part of the vertical and NMO velocity models is more significant than in the corresponding velocity models built by monoparameter FWI with the type 1 parameterization (Figure 14a and 14c). See text for additional discussion.

equation 2, and is kept the same over the iterations. This differs from the regularization that was used for the synthetic experiment, where the prior model was the initial model of the current iteration. We found that, in the presence of noise, L-BFGS optimization was leading to noisy reconstruction if the prior model was modified at each iteration. This results because the L-BFGS algorithm builds the approximate inverse Hessian from several gradients and models obtained at previous iterations and therefore, does not allow for the modification of the misfit function from one iteration to the next. Tikhonov regularization is performed with an exponential function of adaptive correlation lengths of 20% of the local wavelengths, equation 3.

Monoparameter vertical transverse isotropic FWI

We first perform monoparameter VTI FWI to update the vertical velocity, horizontal velocity, and NMO velocity using type 1 parameterization, following the same approach as for the synthetic test. The initial models for FWI are shown in Figure 12. The three FWI velocity models (V_{P0}, V_h, and V_{NMO}) are of comparable quality and resolution (Figure 14). This is consistent with their similar radiation patterns when type 1 parameterization is used (Gholami et al. [2013], their Figure 3b and 3d). Comparison of the FWI vertical velocity model against the well log shows good agreement between the measured and reconstructed vertical velocity (Figure 15).

Multiparameter vertical transverse isotropic FWI

We now perform the joint update of two wave speeds by multiparameter VTI FWI. Two parameterizations are tested: (V_{P0}, δ, V_h) and (V_{NMO}, δ, V_h). The smooth background model of δ is kept fixed during the inversion. The same value of the damping factor λ_i is

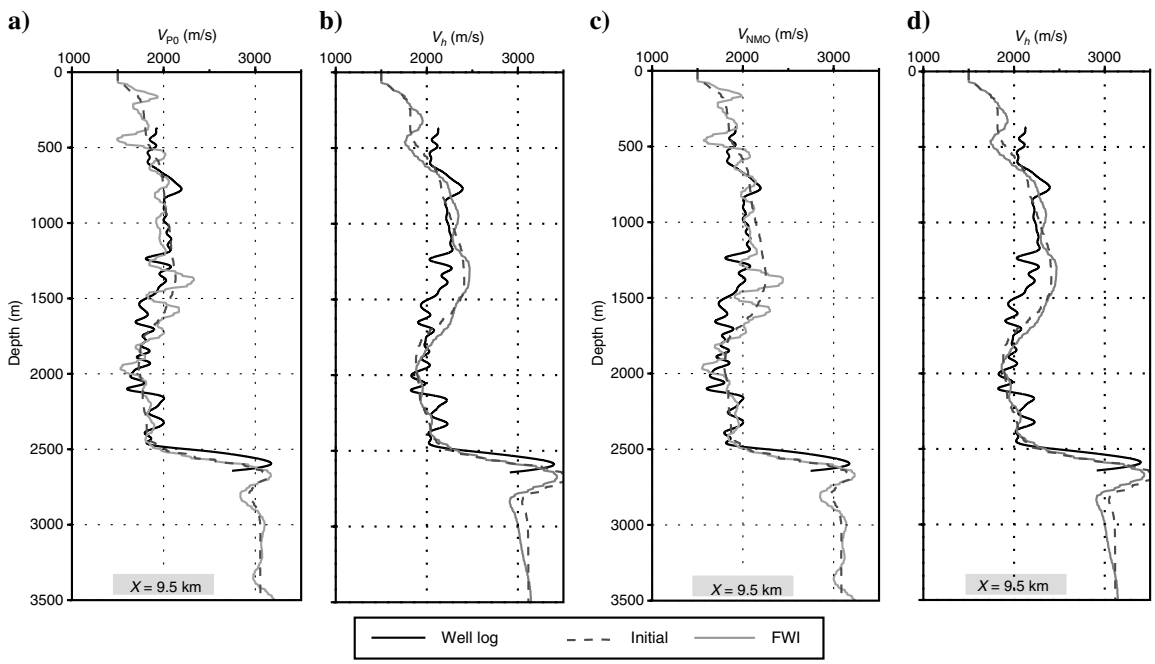

Figure 17. Valhall case study: comparison between the well log (black line) and FWI velocities from Figure 16 (solid gray line). (a, b) Vertical velocity (a) and horizontal velocity (b) (Figure 16a and 16b). (c, d) NMO velocity (c) and horizontal velocity (d) (Figure 16c and 16d). The well log for horizontal velocity and NMO velocity were built with the same procedure as in Figure 15. The logs of the initial models are plotted with dashed gray lines.

used for the two wave speeds, equation 2, as they have radiation pattern of similar amplitudes (Gholami et al. [2013], their Figure 3e and 3f). The final FWI models for the two parameterizations are shown in Figure 16. The vertical velocity model and the NMO velocity model inferred from the two parameterizations are of comparable quality and resolution (Figure 16a, 16c and Figure 17a, 17c), which is consistent because their radiation patterns are similar. These velocity models are also similar to those inferred from monoparameter FWI (Figure 14). Nevertheless, we note some vertical oscillations in the upper part of the vertical and NMO velocity models inferred from multiparameter FWI, and the footprint of these oscillations appears less significant in the velocity models inferred from monoparameter FWI (compare Figure 14a and 14c and Figure 16a and 16c). These vertical oscillations might result from the limited vertical-wavenumber bandwidth of the velocity models. If this interpretation is correct, the higher footprint of the oscillations in multiparameter FWI models is consistent: indeed, the velocity models inferred from type 1 parameterization should have a broader wavenumber content in the upper structure (i.e., where the aperture illumination is broad) than the velocity models inferred from type 2 parameterization because their radiation patterns span over the full range of scattering angles when type 1 parameterization is used (Gholami et al. [2013], their Figure 3b and 3e).

The horizontal velocity models obtained with the (V_{P0},δ,V_h) and (V_{NMO},δ,V_h) parameterizations are very similar (Figures 16b, 16d, 17b, and 17d). They show a more limited resolution than that obtained by monoparameter FWI (Figures 14b and 1b). This is a consistent result because the horizontal velocity has an influence on the wide aperture components of the data only with type 2 parameterization (Gholami et al., 2013, their Figure 3e and 3f). The spatial resolution of the horizontal velocity models (Figure 16b and 16d) is, however, improved relative to that of the initial V_h model (Figure 12b).

Time-domain seismograms computed in the final FWI models computed with the (V_{P0}, δ, ϵ) and (V_{P0}, δ, V_h) parameterizations show good and similar agreement with the recorded data for diving waves and reflected phases (Figure 18).

We compute anisotropic RTM and CIGs in the initial models and in the final FWI models obtained with the (V_{P0}, δ, ϵ) and (V_{P0}, δ, V_h) parameterizations using the same approach as Prieux et al. (2011).

RTM is performed in the frequency domain using the acoustic VTI finite-difference frequency-domain modeling method of Operto et al. (2009) and the gradient of the FWI program of Sourbier et al. (2009a, 2009b), where the data residuals are replaced by the data. Common-offset migrated images were computed by migrating independently each class of offset to generate CIGs before stacking. The range of offsets that is considered for migration ranges from −5 to 5 km. For migration, we use a suitable preprocessed data set in the 5–60-Hz frequency band, where free-surface multiples are removed. The migrated images are displayed with an automatic gain control. As the forward-modeling engine embedded in the RTM code relies on the (V_{P0}, δ, ϵ) parameterization of the subsurface, we infer an ϵ model from the FWI V_{P0} model and the FWI V_h model that were obtained with the (V_{P0}, δ, V_h) parameterization to perform RTM. As the relationship between V_{P0}, V_h, and ϵ is nonlinear and as V_{P0} and V_h have different resolution, this transform might have hampered the quality of the migrated image associated with the type 2 parameterization.

The migration computed in the initial anisotropic model provides a highly accurate image of the subsurface at all depths (Figure 19a), which is supported by fairly flat reflectors in the CIGs (Figure 19d). As for Prieux et al. (2011), the migrated images and the CIGs inferred from the FWI background models show less continuous and flat reflectors than those inferred from the reflection-traveltime tomography background model, except in the first kilometer in depth of the subsurface, where the CIGs computed in the FWI models show flatter events (Figure 20). The highest quality of the RTM image inferred from the initial anisotropic model is expected because the reflection traveltime tomography is optimally designed to focus reflection energy in depth, and should perform well in structural environments like Valhall, where no significant dips are shown. In contrast, high-wavenumbers artifacts might accumulate in the FWI models over the nonlinear iterations, and hamper the continuity of the reflectors reconstructed by migration. Overall, the quality of the two migrated images inferred from the FWI background models is similar. The suspicious undulations of the reflectors in the gas layers highlighted in Figure 19b and 19c might result from errors in the model update due to approximate accounting of anisotropy (Prieux et al., 2011). These undulations are slightly less significant in the migrated image built from the FWI background model obtained with the type 2 parameterization compared to that

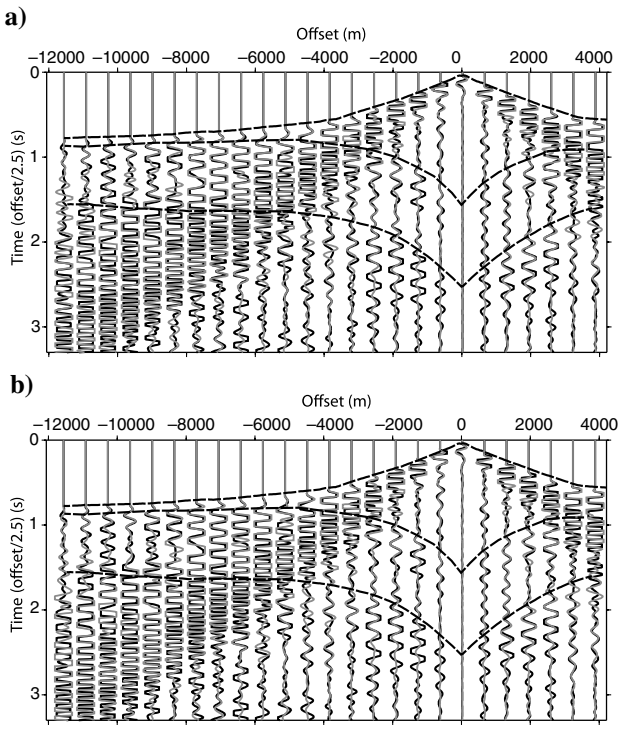

Figure 18. Valhall case study: direct comparison between recorded seismograms (black line) and seismograms computed in the final anisotropic FWI models (gray line). (a) Seismograms are computed in the vertical velocity model updated by monoparameter FWI (Figure 14a) and in the smooth background δ and ϵ models (Figure 12c, 12d). (b) Seismograms are computed in the V_{P0} and V_h models updated by multiparameter FWI (Figure 16a and 16b) and the smooth background δ model (Figure 12c). The dashed black curves are picked first-arrival traveltimes and picked reflection traveltimes from the top and from the bottom of the gas layers.

obtained with the type 1 parameterization (compare Figure 19b, 19e, 19c, and 19f, leftward pointing arrows in the CIGs). This locally leads to flatter CIGs in the gas layers and more continuous image of the top of the reservoir in the migrated image inferred from the (V_{P0}, δ, V_h) parameterization relative to the one inferred from the (V_{P0}, δ, ϵ) parameterization. However, the shallow reflectors above the gas layers and the deep reflector at 3.5 km in depth between 6 and 10 km in distance are generally more continuous in the RTM image inferred from the (V_{P0}, δ, ϵ) parameterization. This comparative analysis of the RTM images inferred from the FWI background models might suggest that the joint update of V_{P0} and V_h might have been helpful to update the subsurface in the gas layers where the initial ϵ might lack accuracy. In contrast, the FWI V_{P0} model inferred from the (V_{P0}, δ, ϵ) parameterization might be more suitable for RTM where the ϵ background is sufficiently accurate (above the gas) or where anisotropy has less effects

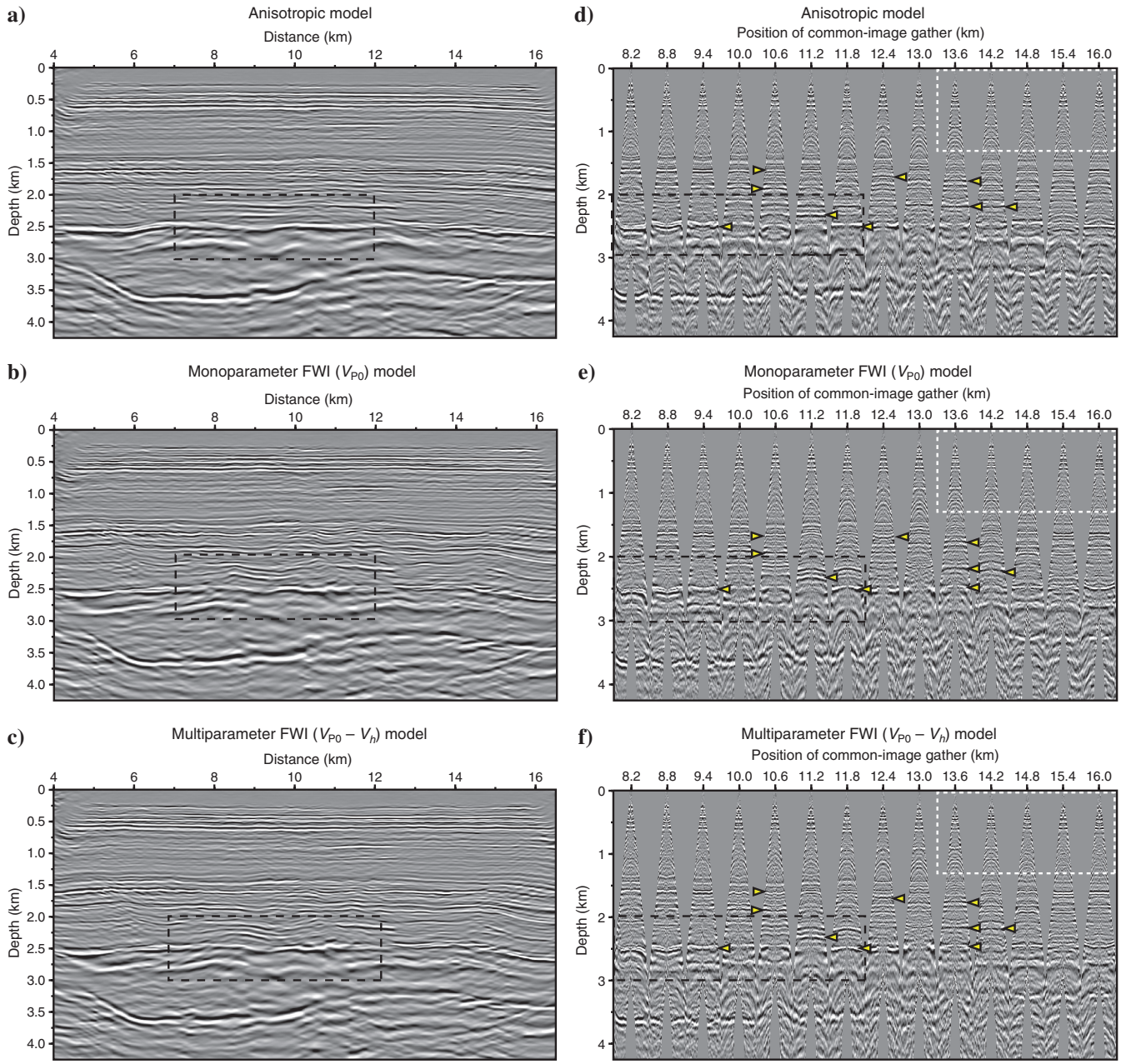

Figure 19. Valhall case study: VTI RTM. (a-c) Migrated images computed in the initial models (a) (Figure 12) and in the anisotropic models updated by monoparameter FWI (b) (Figure 14a) and by multiparameter FWI (c) (Figure 16a and 16b). The frame delineates the area in the migrated images computed in the FWI models, where reflectors show suspicious undulations, similar to those shown in Prieux et al. (2011), their Figure 8e and 8h). (d-f) CIGs computed in the offset-depth domain. Leftward pointing arrows highlight reflectors that are slightly flatter in (f) relatively to (e). Conversely, rightward pointing arrows highlight reflectors that are slightly flatter in the (e) relatively to (f). The dash white box delineates the close-up of the CIGs shown in Figure 20.

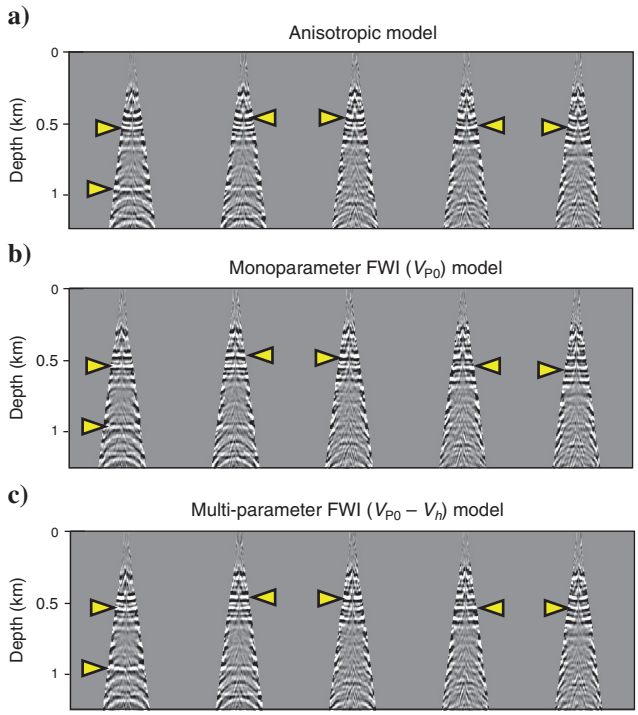

Figure 20. Valhall case study: VTI RTM. Close-up of CIGs shown in Figure 19 centred on the shallow part (dash white box in Figure 19). (a-c) CIGs are computed in the initial models (a), and in the anisotropic models updated by monoparameter FWI (b) (Figure 14a) and by multiparameter FWI (c) (Figure 16a and 16b). Leftward pointing arrows highlight reflectors that are flatter in (c) relatively to (b). Conversely, rightward pointing arrows highlight reflectors that are slightly flatter in the (c) relatively to (b). FWI background models (b, c) improve the migrated image in the shallow part relatively to the initial model (a).

(in the deep part) because a broader range of wavelengths has been updated in the V_{P0} model when (V_{P0}, δ, ϵ) parameterization is used.

CONCLUSION

The FWI case studies presented in this study support the conclusions of the theoretical parameterization analysis of acoustic VTI FWI presented in the companion paper. As long as accurate long-wavelength models of the Thomsen parameters δ and ϵ are developed during the preliminary tomographic step, a high-resolution velocity model (for the vertical, the horizontal, or NMO velocity) can be reconstructed by monoparameter FWI, when the subsurface parameterization combines the wave speed with the two Thomsen parameters. The joint update of the vertical velocity and the parameter ϵ (or, of the NMO velocity and the parameter η) has been shown to be feasible, although this led to a marginal update of the Thomsen parameter, as most of the influence of parameters ϵ or η on the wide-aperture components of the data is predicted by the initial models. Alternatively, the joint update of two wave speeds (the vertical velocity and horizontal velocity, or the NMO velocity and horizontal velocity) shows robust results because the two wave speeds have significant influences on the data for distinct ranges of scattering angles. Hence, trade-off artifacts should not significantly impact on the inversion. The horizontal velocity model has a limited resolution because it has influence on the large scattering angles only, when the horizontal velocity is combined with the vertical velocity or the NMO velocity in the parameterization. The vertical velocity model or the NMO velocity model have a narrower wavenumber content when they are combined with the horizontal velocity rather than with parameter ϵ because they have influence on the data for small and intermediate scattering angles in the former case, whereas they have influence on the data over the full range of scattering angles in the latter case. However, we do not show significant differences in resolution between the vertical velocity models and the NMO velocity models built with the two parameterizations because the long wavelengths of the vertical or NMO velocity models are already present in the starting models. In all of the tests, the background model of Thomsen parameter δ is kept fixed due to its limited influence in the data. We would conclude that the choice of a suitable parameterization for acoustic VTI FWI should be driven by the accuracy of the initial models as well as any prior information which can be used during FWI. If sufficiently accurate large-scale models of the Thomsen parameters are available, we would tend to favor a parameterization that involves only one wave speed to build a high-resolution velocity model of the subsurface. If a sufficiently accurate large-scale model of the vertical velocity is available to predict the kinematic of the short-spread reflections, the parameterization which combines two wave speeds will jointly update the long wavelengths of the horizontal model and the short wavelengths of the vertical velocity with a limited risk of trade-off between the two wave speeds. One advantage of the two-wave speed parameterization is that the inversion regularization and parameter normalization is easy to tune because the two wave speeds have the same range of values and an influence on data of similar strength.

In the framework of multiparameter FWI, a key issue is to account for the Hessian in the optimization. The Hessian seeks to correct for the trade-off between different parameter classes. By trade-off is meant that several classes of parameter can have a coupled influence on the data, that implies that the true model perturbation for one parameter class is a linear combination of the gradients associated with different parameter classes. The L-BFGS quasi-Newton method provides a computationally efficient framework, to take into account the effects of the Hessian in the FWI. More accurate accounting for the Hessian can be, however, obtained with Gauss-Newton or full Newton optimization, which deserve future investigations in the framework of multiparameter FWI. The regularization damping term, conventionally added on the diagonal of the Hessian, can have a large influence on the reconstruction of the parameters. When this damping is scaled to the maximum coefficient of the Hessian, the reconstruction of the parameter with the Fréchet derivatives of highest amplitude is favored at the expense of the secondary parameters. In the present study, we normalize the parameter classes by their mean value in the background medium such that the Fréchet derivatives of the wavefield with respect to these normalized parameters reflect the real physical influence of the parameters on the data. With such normalization, we deliberately steer the inversion toward the parameters that have a strongest influence on the data (i.e., wave speeds) at the expense of the secondary parameters (i.e., Thomsen parameters).

Future work will first aim to account more accurately for the Hessian through Gauss-Newton and full Newton optimization. Second, more carefully design of the regularization of the FWI should allow for an assessment of the feasibility of the reconstruction of multiple

classes of parameters with variable imprints in the data, keeping in mind that the reconstruction of parameters that have an influence below the noise level in the data is unlikely. This improved regularization might allow the joint updating of the vertical velocity and the long wavelengths of parameter ϵ (or the NMO velocity and parameter η), if the available background model of the Thomsen parameter is not accurate enough.

ACKNOWLEDGMENTS

This study was funded by the SEISCOPE consortium http://seiscope.oca.eu, and sponsored by BP, CGG-VERITAS, ENI, EXXON-MOBIL, PETROBRAS, SAUDI ARAMCO, SHELL, STATOIL, and TOTAL. The linear systems were solved with MUMPS package, available on http://graal.ens-lyon.fr/MUMPS/index.html. The mesh generation was performed with help of TRIANGLE, available on http://www.cs.cmu.edu/~quake/triangle.html. Access to the high-performance computing facilities of the SIGAMM (Observatoire de la Côte d'Azur) is acknowledged gratefully. This study was granted access to the HPC resources of [CINES/IDRIS] under the allocation 2010- [project gao2280] of GENCI (Grand Equipement National de Calcul Intensif), and we gratefully acknowledge both of these facilities and the support of their staff. We also thank BP Norge AS and their Valhall partner Hess Norge AS for allowing access to the Valhall data set, as well as the data set preprocessed by PGS for migration, and the well-log velocities. We would like to thank the Associate Editor, Yaxun Tang (ExxonMobil Upstream Research), Dong-Joo Min (Seoul National University), and two anonymous reviewers for their very helpful comments.

REFERENCES

Alkhalifah, T., and I. Tsvankin, 1995, Velocity analysis for transversely isotropic media: Geophysics, **60**, 1550–1566, doi: 10.1190/1.1443888.

Barkved, O., and P. Heavey, 2003, Valhall field — Still on plateau after 20 years of production: Presented at the Conference Offshore Europe, SPE.

Barnes, C., M. Charara, and T. Tsuchiya, 2008, Feasibility study for an anisotropic full waveform inversion of cross-well data: Geophysical Prospecting, **56**, 897–906, doi: 10.1111/j.1365-2478.2008.00702.x.

Brossier, R., 2011, Two-dimensional frequency-domain visco-elastic full waveform inversion: Parallel algorithms, optimization and performance: Computers & Geosciences, **37**, 444–455, doi: 10.1016/j.cageo.2010.09.013.

Brossier, R., Y. Gholami, J. Virieux, and S. Operto, 2010, 2D frequency-domain seismic wave modeling in VTI media based on a Hp-adaptive discontinuous Galerkin method: 72nd Annual International Conference and Exhibition, EAGE, Extended Abstracts, C046.

Brossier, R., S. Operto, and J. Virieux, 2009, Seismic imaging of complex onshore structures by 2D elastic frequency-domain full-waveform inversion: Geophysics, **74**, no. 6, WCC105–WCC118, doi: 10.1190/1.3215771.

Brossier, R., J. Virieux, and S. Operto, 2008, Parsimonious finite-volume frequency-domain method for 2-D *P-SV*-wave modelling: Geophysical Journal International, **175**, 541–559, doi: 10.1111/j.1365-246X.2008.03839.x.

Gardner, G. H. F., L. W. Gardner, and A. R. Gregory, 1974, Formation velocity and density–the diagnostic basics for stratigraphic traps: Geophysics, **39**, 770–780, doi: 10.1190/1.1440465.

Gholami, Y., R. Brossier, S. Operto, A. Ribodetti, and J. Virieux, 2013, Which parameterization is suitable for acoustic vertical transverse isotropic full waveform inversion? Part 1: Sensitivity and trade-off analysis: Geophysics, **78**, this issue, doi: 10.1190/geo2012-0204.1.

Ji, Y., and S. Singh, 2005, Anisotropy from full waveform inversion of multicomponent seismic data using a hybrid optimization method: Geophysical Prospecting, **53**, 435–445, doi: 10.1111/j.1365-2478.2005.00476.x.

Kommedal, J. H., O. I. Barkved, and D. J. Howe, 2004, Initial experience operating a permanent 4C seabed array for reservoir monitoring at Valhall: 74th Annual International Meeting, SEG, Expanded Abstracts, 2239–2242.

Kommedal, J. H., O. I. Barkved, and L. A. Thomsen, 1997, Acquisition of 4 component OBS data — A case study from the Valhall field: 59th Annual International Conference and Exhibition, EAGE, Extended Abstracts, B047.

Lee, H.-Y., J. M. Koo, D.-J. Min, B.-D. Kwon, and H. S. Yoo, 2010, Frequency-domain elastic full-waveform inversion for VTI media: Geophysical Journal International, **183**, 884–904, doi: 10.1111/j.1365-246X.2010.04767.x.

Leonard, R., and J. Munns, 1987, Valhall field in geology of Norwegian oil and gas fields: Graham and Trotman.

Munns, J. W., 1985, The Valhall field: A geological overview: Marine and Petroleum Geology, **2**, 23–43, doi: 10.1016/0264-8172(85)90046-7.

Nocedal, J., 1980, Updating quasi-Newton matrices with limited storage: Mathematics of Computation, **35**, 773–782, doi: 10.1090/S0025-5718-1980-0572855-7.

Operto, S., J. Virieux, A. Ribodetti, and J. E. Anderson, 2009, Finite-difference frequency-domain modeling of visco-acoustic wave propagation in two-dimensional TTI media: Geophysics, **74**, no. 5, T75–T95, doi: 10.1190/1.3157243.

Plessix, R. E., 2006, A review of the adjoint-state method for computing the gradient of a functional with geophysical applications: Geophysical Journal International, **167**, 495–503, doi: 10.1111/j.1365-246X.2006.02978.x.

Plessix, R. E., and Q. Cao, 2011, A parametrization study for surface seismic full waveform inversion in an acoustic vertical transversely isotropic medium: Geophysical Journal International, **185**, 539–556, doi: 10.1111/j.1365-246X.2011.04957.x.

Plessix, R. E., and C. Perkins, 2010, Full waveform inversion of a deep water ocean bottom seismometer data set: First Break, **28**, 71–78.

Podvin, P., and I. Lecomte, 1991, Finite difference computation of traveltimes in very contrasted velocity model: A massively parallel approach and its associated tools: Geophysical Journal International, **105**, 271–284, doi: 10.1111/j.1365-246X.1991.tb03461.x.

Pratt, R. G., 1999, Seismic waveform inversion in the frequency domain, part I : Theory and verification in a physic scale model: Geophysics, **64**, 888–901, doi: 10.1190/1.1444597.

Pratt, R. G., C. Shin, and G. J. Hicks, 1998, Gauss-Newton and full Newton methods in frequency-space seismic waveform inversion: Geophysical Journal International, **133**, 341–362, doi: 10.1046/j.1365-246X.1998.00498.x.

Prieux, V., R. Brossier, Y. Gholami, S. Operto, J. Virieux, O. Barkved, and J. Kommedal, 2011, On the footprint of anisotropy on isotropic full waveform inversion: The Valhall case study: Geophysical Journal International, **187**, 1495–1515, doi: 10.1111/j.1365-246X.2011.05209.x.

Robertson, J. O. A., K. Holliger, A. G. Green, A. Pugin, and R. D. Iaco, 1996, Effects of near-surface waveguides on shallow high-resolution seismic refraction and reflection data: Geophysical Research Letters, **23**, 495–498, doi: 10.1029/96GL00384.

Sirgue, L., O. I. Barkved, J. Dellinger, J. Etgen, U. Albertin, and J. H. Kommedal, 2010, Full waveform inversion: The next leap forward in imaging at Valhall: First Break, **28**, 65–70.

Sourbier, F., S. Operto, J. Virieux, P. Amestoy, and J.-Y. L'Excellent, 2009a, FWT2D: A massively parallel program for frequency-domain full-waveform tomography of wide-aperture seismic data — Part 1: Algorithm: Computers & Geosciences, **35**, 487–495, doi: 10.1016/j.cageo.2008.04.013.

Sourbier, F., S. Operto, J. Virieux, P. Amestoy, and J.-Y. L'Excellent, 2009b, FWT2D: A massively parallel program for frequency-domain full-waveform tomography of wide-aperture seismic data — Part 2: Numerical examples and scalability analysis: Computers & Geosciences, **35**, 496–514, doi: 10.1016/j.cageo.2008.04.012.

Tarantola, A., 1987, Inverse problem theory: Methods for data fitting and model parameter estimation: Elsevier.

Thomsen, L. A., 1986, Weak elastic anisotropy: Geophysics, **51**, 1954–1966, doi: 10.1190/1.1442051.

Thomsen, L. A., O. Barkved, B. Haggard, J. H. Kommedal, and B. Rosland, 1997, Converted-wave imaging of Valhall reservoir: 59th Annual International Conference and Exhibition, EAGE, Extended Abstracts, B048.

Tikhonov, A., and V. Arsenin, 1977, Solution of ill-posed problems: Winston.

Vigh, D., B. Starr, J. Kapoor, and H. Li, 2010, 3D full waveform inversion on a Gulf of Mexico WAZ data set: 80th Annual International Meeting, SEG, Expanded Abstracts, 957–961.

Virieux, J., and S. Operto, 2009, An overview of full waveform inversion in exploration geophysics: Geophysics, **74**, no. 6, WCC1–WCC26, doi: 10.1190/1.3238367.